Spectroscopy and Kinetics of Wild-Type and Mutant Tyrosine Hydroxylase: Mechanistic Insight into O-2 Activation

7 AUTHORS, INCLUDING:

Paul F Fitzpatrick

University of Texas Health Science Center at …

197 PUBLICATIONS   **4,525** CITATIONS

Spectroscopy and Kinetics of Wild-Type and Mutant Tyrosine Hydroxylase: Mechanistic Insight into O₂ Activation

Marina S. Chow[†], **Bekir E. Eser**[§], **Samuel A. Wilson**[†], **Keith O. Hodgson**[*,†,‡], **Britt Hedman**[*,‡], **Paul F. Fitzpatrick**[*,§], and **Edward I. Solomon**[*,†]

Contribution from the Department of Chemistry, Stanford University, Stanford, CA 94305, Stanford Synchrotron Radiation Laboratory, SLAC, Stanford University, Stanford 94309, and Department of Biochemistry and Biophysics, and Department of Chemistry, Texas A&M University, College Station, Texas 77843

Abstract

Tyrosine Hydroxylase (TH) is a pterin-dependent non-heme iron enzyme that catalyzes the hydroxylation of L-tyr to L-DOPA in the rate-limiting step of catecholamine neurotransmitter biosynthesis. We have previously shown that the Fe^{II} site in Phenylalanine Hydroxylase (PAH) converts from 6C to 5C only when both substrate + cofactor are bound. However, steady-state kinetics indicate that TH has a different cosubstrate binding sequence (pterin + O_2 + L-tyr) than PAH (L-phe + pterin + O_2). Using x-ray absorption spectroscopy (XAS), and variable-temperature-variable-field magnetic circular dichroism (VTVH MCD) spectroscopy, we have investigated the geometric and electronic structure of the WT TH and two mutants, S395A and E332A, and their interactions with substrates. All three forms of TH undergo 6C → 5C conversion with tyr + pterin, consistent with the general mechanistic strategy established for O_2-activating non-heme iron enzymes. We have also applied single-turnover kinetic experiments with spectroscopic data to evaluate the mechanism of the O_2 and pterin reactions in TH. When the Fe^{II} site is 6C, the two-electron reduction of O_2 to peroxide by Fe^{II} and pterin is favored over individual one-electron reactions, demonstrating that both a 5C Fe^{II} and a redox-active pterin are required for coupled O_2 reaction. When the Fe^{II} is 5C, the O_2 reaction is accelerated by at least 2 orders of magnitude. Comparison of the kinetics of WT TH, which produces Fe^{IV}=O + 4a-OH-pterin, and E332A TH, which does not, shows that the E332 residue plays an important role in directing the protonation of the bridged Fe^{II}-OO-pterin intermediate in WT to productively form Fe^{IV}=O, which is responsible for hydroxylating L-tyr to L-DOPA.

1 Introduction

Mononuclear non-heme iron enzymes catalyze a wide variety of reactions involving O_2. Tyrosine Hydroxylase (TH, EC 1.14.16.2) belongs to the family of enzymes that utilize Fe^{II} and a pterin cofactor to activate dioxygen for aromatic amino acid hydroxylation (Scheme 1).[1–3] In humans, TH is found in the central and peripheral nervous systems and catalyzes the rate-limiting step in catecholamine neurotransmitter biosynthesis by converting L-tyrosine into L-DOPA. L-DOPA is subsequently converted to dopamine, norepinephrine and epinephrine,

E-mail: E-mail: edward.solomon@stanford.edu; E-mail: fitzpat@tamu.edu; E-mail: hedman@ssrl.slac.stanford.edu; E-mail: hodgson@ssrl.slac.stanford.edu.
[†]Department of Chemistry, Stanford University
[‡]Stanford Synchrotron Radiation Laboratory
[§]Department of Biochemistry & Biophysics, and Department of Chemistry, Texas A&M University

which play key roles in regulating motor-coordination, behavior, learning and memory, sleep-wake cycle and the stress response. Dysfunction of this enzyme has been linked to several neurological disorders including Parkinson's disease,[4] bipolar disorder,[5] and Segawa's syndrome.[6,7] The other two pterin-dependent hydroxylases also play key roles in proper neurofunction: Phenylalanine Hydroxylase (PAH) converts phenylalanine into tyrosine, and its dysfunction results in severe mental retardation (phenylketonuria, PKU).[8,9] Tryptophan Hydroxylase makes 5-hydroxytryptophan in the first step of serotonin biosynthesis and plays an important role in mood regulation.[10]

In bacterial PAH the cosubstrates are reported to bind in a specific order – phenylalanine, then pterin, and finally O_2, for productive enzyme turnover,[11] although there is some uncertainty in this.[12] Using magnetic circular dichroism (MCD) and x-ray absorption spectroscopies (XAS), we have found that the resting ferrous site of rat PAH is 6-coordinate (6C).[13] Binding of either phenylalanine or 5-deaza-6-methyltetrahydropterin (5-deaza-6MPH$_4$) only slightly perturbs the 6C Fe^{II} site, whereas binding of L-phe + 5-deaza-6MPH$_4$ converts the site to 5-coordinate (5C) through the loss of a water ligand, and opens a coordination position for O_2 to react.[14,15] This structural change at the PAH active site was subsequently observed by crystallography.[16,17] The crystal structures showed that the resting 6C Fe^{II} site was coordinated by 2 histidines (His), 1 glutamate (Glu) and 3 waters. When substrate analogs (norleucine or thienylalanine) and cofactor are bound, the Fe^{II} site becomes 5C, with the Glu binding in a bidentate fashion.

A different sequence of co-substrate binding was observed with steady-state kinetics in TH, where the order is first pterin, followed by O_2 and then tyrosine before product release.[18] In fact, the binding of tyrosine to Fe^{II}TH results in a dead end complex. These findings suggest that the Fe^{II} active site in TH might undergo a different structural mechanism as compared to PAH, even though the enzymes share high sequence homology [3] and perform similar reactions. However, there is limited structural information available on TH. The two crystal structures of TH are of the enzyme in the ferric form, one in resting state (1TOH) and the other with oxidized cofactor, 7,8-dihydrobiopterin, bound (2TOH).[19,20] Both of these structures show a five-coordinate Fe^{III} site, with 2 His, 1 Glu and 2 water ligands; the presence of oxidized pterin did not affect the structure of the active site. Mössbauer studies on TH confirmed that the Fe^{II} is high spin S = 2, and XAS studies on the resting Fe^{II}TH and Fe^{II}TH + tetrahydrobiopterin (BH$_4$) indicate that both sites are 6C.[21] The electron paramagnetic resonance (EPR) spectrum of Fe^{III}TH is characteristic of a high-spin, predominantly rhombic site.[22] At present, there is no structural information on catalytically relevant Fe^{II}TH with tyrosine or tyrosine + pterin bound.

When both pterin and tyrosine are present, TH catalyzes the dioxygen dependent hydroxylation of both molecules (Scheme 1). The O_2 molecule is partitioned between the hydroxylated substrate and cofactor,[23–25] leading to the proposed formation of a putative Fe^{II}-peroxy-pterin intermediate (Fe^{II}-OO-pterin),[24] which undergoes heterolytic O-O bond cleavage to give the hydroxylating intermediate Fe^{IV}=O and a 4a-hydroxy-pterin adduct (4a-OH-pterin). The Fe^{IV}=O intermediate in TH was recently trapped and studied using Mössbauer spectroscopy.[26] The 4a-OH-pterin subsequently dehydrates to produce quinonoid pterin.

Although a mechanism for the formation of the Fe^{IV}=O hydroxylating intermediate has been proposed and generally accepted,[27–29] earlier steps in the pterin-dependent reaction, specifically the steps leading to the formation of the putative Fe^{II}-OO-pterin intermediate, are still poorly understood (Scheme 2). In a computational study, Siegbahn and colleagues have proposed that O_2 first reacts with Fe^{II} to form a Fe^{3+}-$O_2^{-\bullet}$ complex.[30] However, this process is thermodynamically unfavorable by ~ 20 kcal/mol.[31] In contrast, spectroscopic and kinetic

studies on two PAH mutants suggested a different mechanism in which O_2 reacts first with pterin to form a peroxy-pterin species (HOO-pterin) before bridging to Fe^{II}.[32]

In this study, Fe K-edge XAS edge and EXAFS (extended x-ray absorption fine structure) spectroscopy combined with near-IR MCD and variable-temperature-variable-field MCD (VTVH MCD) are applied to investigate the geometric and electronic structure changes of the Fe^{II}TH active site and the effects of tyrosine and pterin binding. We also studied two mutants of TH that have different reactivity towards the pterin cofactor to correlate these differences in reactivity to active site structural differences. The homologous mutations in PAH have been shown to result in PKU.[33,34] The S395A mutant produces 4a-OH-pterin at the same rate as WT, but does so in predominantly uncoupled reaction (2% of WT tyrosine hydroxylation). [35] The S395 residue in TH hydrogen-bonds to the His336 Fe^{II} ligand and is in the vicinity of the tyrosine binding pocket. The E332A mutant hydroxylates less than 1% tyrosine compared to WT and does not produce 4a-OH-pterin.[36] The E332 residue is hydrogen-bonded to the first sphere ligand His331 as well as to the pterin cofactor. Together, these mutants probe the mechanism of the oxygen/pterin reaction in TH. These results are correlated to the results of new single-turnover kinetic studies on WT TH and the E332A mutant to evaluate the mechanisms of O_2 reaction, formation of a bridged species, and O-O cleavage.

2 Materials and Methods

2.1 Protein expression: Wild-type and Mutants

Wild-type (WT), E332A and S395A rat TH were overexpressed in *E. coli* and purified as previously described.[35–37] After purification, the enzyme was precipitated with 70% ammonium sulfate and dissolved in deuterated MOPS/KCl buffer, pD=7.3, (containing either 5 mM EDTA for WT and E332A or 1 equiv of ferrous ammonium sulfate, $Fe(NH_4)_2SO_4$, per monomer for S395A), followed by dialysis against the same buffer. Glycerol-d_3 was then added during concentration steps to give final buffer conditions of 100 mM MOPS, pD=7.3, 65% glycerol-d_3 and 300 mM KCl. Iron contents were determined using a Perkin-Elmer Analyst 700 atomic absorption spectrophotometer.[38]

2.2 Preparation of XAS and MCD Samples

All commercial reagents were of the highest grade and used without further purification. Solutions were made anaerobic either by ten freeze-pump-thaw cycles or by purging with argon on a schlenk line. Solids were purged with argon for 1–2 hours. Anaerobic reagents were transferred into a nitrogen atmosphere maintained in a Vacuum Atmosphere Nexus-1 glovebox (< 5 ppm oxygen). $Fe(NH_4)_2SO_4$ (J.T. Baker) and sodium dithionite (Sigma-Aldrich) were dissolved in anaerobic D_2O (99.9 atom % D). 6-Methyltetrahydropterin (6MPH$_4$, Schircks Laboratories) was dissolved in an anaerobic solution of 10 mM HCl. The concentration of the 6MPH$_4$ stock solution was determined from the absorbance at 266 nm (ε_{266nm} = 17.8 mM^{-1}cm^{-1}). The redox inactive cofactor 5-deaza-6MPH$_4$ was synthesized according to literature procedures.[39] Concentrated solutions of L-tyrosine (L-tyr) were prepared in D_2O adjusted to pD = 10 using NaOD.

Enzyme samples were made anaerobic by purging with argon. In the glovebox, approximately 0.85 equiv of $Fe(NH_4)_2SO_4$ was added to the enzyme, followed by five reducing equiv of dithionite solution. The Fe^{II}-TH samples were incubated for 10 minutes, then tyrosine and 6MPH$_4$ were added as needed and the samples incubated for another 10 to 20 minutes. Samples for XAS experiments were each syringed into Lucite $23 \times 2 \times 3$ mm pinhole type XAS cells with 37 μm Kapton windows. MCD samples were injected into an MCD cell, which consists of two Infrasil quartz disks (Esco Products) separated by a neoprene spacer (0.3 cm pathlength)

and held in place by two fitted copper plates. After removal from the glovebox, the XAS and MCD samples were quickly frozen in liquid nitrogen and stored at 77K.

Samples for spectroscopy included TH-[ ], TH-[L-tyr], TH-[6MPH$_4$], TH-[5-deaza-6MPH$_4$] and TH-[L-tyr, 6MPH$_4$] and typically contained 0.8–2 mM FeII, 2–5 mM tyrosine, 3–5 mM 6MPH$_4$ (or 5-deaza-6MPH$_4$) and approximately 60% v/v glycerol-d_3.

2.3 XAS

X-ray absorption spectra were recorded at the Stanford Synchrotron Radiation Laboratory (SSRL) on beam lines 7–3 [40] and 9–3 [41] over an energy range of 6785 to 8000 eV ($k = 15$ Å^{-1}). Hutch slits were set at 2×10 mm and 1×4 mm on beam lines 7–3 and 9–3 respectively, with the first inflection point of the Fe foil set to 7111.2 eV as an internal calibration.[42] Fluorescence data were collected using a solid-state 30-element Ge detector[43] with a Mn filter and Soller slits aligned at 90°, with sample orientated at 45° to incident beam. Sample cryogenic temperature of 10K was maintained using an Oxford Instruments CF1208 continuous-flow liquid helium cryostat. Data collection was continuously monitored in order to ensure sample integrity by averaging blocks of two scans and comparing to the other previous averages. No sample degradation was observed in the edge or EXAFS data in any of the samples, thus all scans were used in the final average. Total scan numbers varied based on sample concentration and desired data quality resulting in 22, 31, 39, and 20 scans for TH-[ ], TH-[L-tyr], TH-[6MPH$_4$], and TH-[L-tyr, 6MPH$_4$] respectively. Reduction and normalization of the data was performed according to established methods[44–46] using the program PySpline[47] for background subtraction and spline fitting. In order to compare multiple data sets, the full data set was truncated to $k= 9.5$ Å^{-1} for pre-edge and edge analysis. The pre-edge data ($k = 9.5$ Å^{-1}) were normalized using a third-order post-edge polynomial background and a two-segment spline. For the EXAFS data ($k = 15$ Å^{-1}) a second-order post-edge polynomial and three-segment spline was used in order to normalize the data.

Using the fitting program EDG_FIT,[48] pre-edge features were successfully modeled using a pseudo-Voigt line shape in a 50:50 ratio of Lorentzian:Gaussian functions. The energy position, full width at half-maximum (FWHM), and peak intensity were all allowed to vary throughout the fitting process. A function modeling the background was empirically chosen to give the best fit. For a fit to be acceptable it had to reasonably match both the pre-edge data as well as that of the second derivative. In all cases three acceptable fits with different FWHM (± 0.5 fixed from float) backgrounds were acquired over the energy ranges of 7108–7116, 7108–7117, and 7108–7118 eV resulting in a total of nine pre-edge fits per data set, which were averaged to get mean values. Standard deviations for the peak energies and intensities from the successful pre-edge fits were used to quantify the error.

EXAFS signals were calculated using FEFF (version 7.0) and a ferric tyrosine hydroxylase crystal structure truncated to an iron ligated by two waters, two His and one Glu. The starting crystal structure (PDB ID 1TOH)[49] was then modified with either the addition of a water ligand to make a 6C model, or modification of the Glu to bind in a bidentate fashion in order to achieve a final fit. The models were fit using OPT as part of the program suite EXAFSPAK[50] by allowing the bond lengths (R) and bond variance (σ^2) to float. The shift in threshold energy ($k = 0$, E$_0$) was also varied but constrained as a common variable (ΔE$_0$) for all fit paths for a given data set. The amplitude reduction factors (S$_0$2) was fixed to a value of 1.0 and coordination numbers (N) were varied systematically to accomplish the best fit to the data based on the model. All samples fit reasonably well using a combination of 4 or 5 paths except for TH[L-tyr, 6MPH$_4$] which required two additional paths. First coordination spheres were fit using a nitrogen backscatter, with a nitrogen/oxygen mix chosen in cases with a split first shell. As oxygen and nitrogen are indistinguishable by EXAFS, best first shell fits were chosen on the basis of normalized error (F) for all the available paths. Second and outer shell fits were

again chosen on the basis of best normalized error (F) for all available paths resulting in the use of carbon single scattering and carbon multiple scattering through the His rings. σ^2 values were set to initial values of 0.005 Å^2 and then allowed to float in all fits, even for those where single scattering and multiple scattering paths were related to one another. The best overall fit was evaluated based on comparison of the normalized error (F) for each proposed fit and by inspection of the fit to the EXAFS to the data, Fourier transform and individual EXAFS wave components. Based on EXAFS studies of known complexes, the uncertainties in final distances are within 0.02 Å.

2.4 MCD Spectroscopy

Low temperature near-IR MCD data were collected on a Jasco J200D spectropolarimeter (600 – 2000 nm) equipped with a liquid nitrogen-cooled InSb photodiode detector and fitted with an Oxford Instruments SM 4000-7T superconducting magnet along the beam path. MCD spectra were corrected for zero-field baseline effects either by subtracting the corresponding 0T scan or by averaging the positive and negative field data at each temperature. Gaussian fitting of the MCD spectra was performed using the program PeakFit (SPSS Science). VTVH MCD data were collected at 8 temperatures between 1.6 K and 25 K and at 12 fields between 0 T and 7 T.

2.5 Single Turnover Kinetics

Single turnover reactions of WT TH and E332A TH were monitored using an Applied Photophysics SX20 stopped-flow spectrophotometer in single wavelength absorbance mode. The stopped-flow instrument was made anaerobic by incubation with a solution of sodium dithionite for at least two hours. Anaerobic solutions of $Fe^{II}TH$ (with or without substrates) were mixed with oxygen-saturated buffer (200 mM HEPES, pH 7.5, 10% glycerol and 0.1M KCl) at 5 °C. Solutions of apoenzyme (100–300 μM in 200 mM HEPES, pH 7.5, 10% glycerol and 0.1 M KCl) were made anaerobic in a tonometer using at least 20 argon-vacuum cycles, ferrous ammonium sulfate and substrate solutions were then added under argon. Different oxygen concentrations in buffers were achieved by using a modified MaxBlend medical oxygen blender (Maxtec) to mix argon and oxygen in different ratios and then bubbling through buffer-containing syringes on ice for at least 15 min.

Single wavelength absorbance changes consisted of one or more exponential kinetic phases, which were analyzed by first fitting to single or multiple exponentials using the program KaleidaGraph (Synergy Software); results from these fits were than taken as initial estimates for global fits and simulations. Initial values for k_{on} and k_{off} of the reversible oxygen complex formation steps and estimates for unknown extinction coefficients were determined by global fitting of multiple traces (obtained at multiple wavelengths for varying O_2 concentrations) using the program DynaFit.[51] Initial concentrations were allowed to float within 10% of the experimental values. Global fitting process was performed in an iterative fashion, in which one or two parameters were varied at a time and the rest of the parameters were kept constant. Best fit parameters obtained this way were than employed for the kinetic simulation (DynaFit) of the experimental data to appropriate mechanisms.

3 Results and Analysis

3.1 X-ray Absorption Spectroscopy

Pre-edge—The XAS Fe-K pre-edge feature at ~ 7112 eV, while formally a 1s → 3d electric dipole forbidden transition, gains intensity through the weaker electric quadrupole mechanism, resulting in some pre-edge intensity for centrosymmetric complexes. In lower symmetry, the metal 3d and 4p orbitals mix, and the pre-edge feature increases in intensity through the much larger electric dipole allowed 1s → 4p character.[52] As a result, XAS pre-edge features are very

sensitive to coordination number and geometry.[52,53] For a typical ferrous model complex in a 6C environment, pre-edge intensities average about 4 units, whereas 5C structures average 12 to 13 intensity units.[52] For a protein environment as in TH, pre-edge intensities for a 6C structure are larger than in symmetric model complexes due to variations in ligation, bond lengths and angles.

The pre-edge and edge spectra of four TH complexes are shown in Figure 1. The pre-edge energies and intensities for the four TH complexes listed in Table 1. The normalized data for TH-[ ] (resting, in red), TH-[L-tyr] (substrate, in blue) and TH-[6MPH$_4$] (cofactor, in orange) all look very similar with respect to pre-edge shape and intensity. When both cofactor and substrate are present, TH-[L-tyr, 6MPH$_4$] (green), the pre-edge shows a notable increase in intensity as well as a shift to lower energy both of which are reflected in the second derivative (Figure 1, inset). A difference is also observed in the edge slope as well as the maximum intensity of the rising edge. Small differences are also observed at higher energies above the edge (7150 eV in Figure 1), suggesting that a structural change has occurred when both substrate and cofactor are bound to TH.

For TH-[ ], the pre-edge region was accurately fit using two features at 7112.0 and 7113.8 eV with intensities of 4.4 and 3.9, respectively, for a total intensity of 8.3 units. TH-[L-tyr] and TH-[6MPH$_4$] were both fit with two features at 7111.9 and 7112.8 eV with total intensities of 8.5 and 8.2 respectively. While the total intensities for TH-[ ], TH-[6MPH$_4$], and TH-[L-tyr] are greater than that which is typical for O$_h$ 6C model complexes with uniform ligation, they are similar to those found for 6C structures in Fe^{II} metalloenzymes.[13,21,32,54]

When both substrate and cofactor are present, the total pre-edge intensity of TH-[L-tyr, 6MPH$_4$] increases to 12.5 units, and is fit using two bands at slightly lower energies, 7111.8 and 7113.5 eV with 6.4 and 6.1 intensity units, respectively. This is similar to the 4 units of intensity increase observed in model complexes in going from 6C to 5C, which distorts the ligand field of the Fe^{II} and increases 4p mixing.

EXAFS—EXAFS data and the corresponding Fourier transform (FT) are shown in Figure 2. The intensity of the EXAFS beat pattern of TH-[ ] (red) and TH-[6MPH$_4$] (orange) are very similar with respect to the wave minima and maxima contributing to a first shell FT with the same intensity and position. When only substrate is present, an increase in the EXAFS signal is observed (TH-[L-tyr], Figure 2, blue). This increase in EXAFS amplitude is represented in the FT with an increase of about 20% (from 0.98 to 1.16 units) relative to TH-[ ] and TH-[6MPH$_4$]. Upon binding of both substrate and cofactor, TH-[L-tyr, 6MPH$_4$], shows both a decrease in the EXAFS amplitude as well as a slight shift to higher k. There are also subtle differences in the beat pattern including an additional feature at $k = 8.5$ Å^{-1}. The EXAFS amplitude reduction, and shift in k are also reflected in the FT as the first shell signal decreases from 0.98 in resting to 0.61, and shifts toward shorter bond distances.

EXAFS data for all samples were collected to $k = 15$ Å^{-1}; however, depending on data quality, fits were performed to $k = 14$ Å^{-1}, $k = 13$ Å^{-1}, $k = 14$ Å^{-1}, and $k = 12$ Å^{-1} for TH-[ ], TH-[L-tyr], TH-[6MPH$_4$] and TH-[L-tyr, 6MPH$_4$], respectively. All spectra were fit to both 5C and 6C models, which were built based on the ferric crystal structure of tyrosine hydroxylase (PDB 1TOH [49]). Since a bidentate Glu has been observed in PAH-[L-phe, pterin],[16] TH-[L-tyr, 6MPH$_4$] was also fit to a 5C model with a bidentate Glu. Both 6 and 5C EXAFS models and associated fitting paths are shown in Figure 3. Values for the most relevant EXAFS fits are presented in Table 2, with additional fits given in the Supporting Information.

The EXAFS spectrum for TH-[ ] is fit equally well using a 6C model with 4 or 5 paths in a 6 or 5 + 1 first shell distribution (fits 1 and 3 in Table 2). The pre-edge data for TH-[ ] (shown

above) also indicate that the iron site is 6C, and this finding is supported by MCD data (*vide infra*). The outer shell was successfully fit using the remaining carbon single scattering at 3.12 Å and 4.08 Å and multiple scattering at 4.39 Å from the two histidine (His) rings.

Fits to the EXAFS data when only cofactor is bound (TH-[6MPH$_4$]) are very similar to those of TH-[ ]. The best fit to the data is with a 6 coordinate split first shell, in a 1:5 ratio (fit 9) with the shorter bond distance at ~ 2.1 Å and longer bond distances at ~ 2.2 Å. The outer shell is again successfully fit using only the single and multiple scattering from the His rings. When only substrate is bound, the short bond distance which is seen in TH-[ ] and TH-[6MPH$_4$] is no longer observed in the fit of the EXAFS signal of TH-[L-tyr] (fit 6). However, despite the lower error value which results with the addition of a split first shell, a path difference of 0.02 Å is beyond the resolution with data to $k =13$ Å^{-1}. Thus, the best fit is 4 in which all ligands are incorporated into one 6C shell at 2.16 Å. A symmetric first shell with no resolvable short bond length is consistent with an increase in EXAFS amplitude, as the symmetric shell would provide for a stronger, more uniform signal. This increase is similar to the behavior observed for PAH when the substrate L-phe is present.[13] For all three samples, when the data are fit using only 5 backscatters in the first shell rather than 6, a decrease in σ^2 value is observed and the F factor increases, indicating a worse fit to the data, wit the smallest effect observed for TH-[ ]. This result is similar to previously reported results for TH-[ ] and TH-[BH$_4$], where both forms of the enzyme were observed to contain a 6C first shell.[21] Thus, TH-[ ], TH-[6MPH$_4$] and TH-[L-tyr] forms of tyrosine hydroxylase all contain a distorted 6C site.

For TH-[L-tyr, 6MPH$_4$], a fit using 6 ligands in the first shell results in a σ^2 value which is unreasonably large for bond lengths averaging 2.13 Å (Supporting Information Table S2, fit 10) indicating that the data would be better fit with a 5C first shell. Changing the coordination from 6 to 5 also results in a better overall goodness of fit. A split first shell in a 1:4 ratio with bond lengths of 2.00 and 2.15 Å gives a reasonably good fit (Figure 4 and Table 2, fit 12). However, even with the 1:4 split shell, and the outer shell fit in a similar fashion to those for the other tyrosine hydroxylase samples (2 SS and 1 MS carbon paths at ~ 3.1, 4.1, and 4.4 Å respectively; Table 2, fit 12), at least one wave is still present in the residual signal from the EXAFS fit (Figure 4). An additional single scattering wave at 2.53 Å and an accompanying multiple-scattering wave at 2.65 Å were needed to complete the fit, which now has a 2:3 split in the first shell (Figure 4 and Table 2, fit 15). The residual wave is available if the Glu has shifted into a bidentate coordination mode (Figure 4). None of the other TH complexes required an additional signal at ~ 2.5 Å to complete the fit. To test if a His ligand was lost to form the 5C complex, the outer shell signals from the His were halved. This led to unreasonably low σ^2 values, indicating that the data do not support His dissociation (Supporting Information Table S2, fits 7 and 8). The data indicate that the ligands which were lost are water, similar to the behavior observed in PAH.[15] The *k*-space data and best fit for all complexes can be found in Supporting Information Figure S3.

3.2 MCD Spectroscopy

Wild-type Tyrosine Hydroxylase—The high spin Fe^{2+} (d6) free ion has a ^{5}D ground state, which splits in an octahedral (O$_h$) ligand field into a triply degenerate ^{5}T$_{2g}$ ground state and a doubly degenerate ^{5}E$_g$ excited state, which are separated by 10 *Dq* (~ 10,000 cm^{-1} for O and N ligands). The transitions are very weak in absorption, but are intense at low temperature in MCD. The Fe sites in proteins have lower symmetry which removes the orbital degeneracy of these states. Hence LF transitions to the two components of the ^{5}E$_g$ excited state are observed. For a distorted 6C site, two transitions centered around 10 000 cm^{-1} split by ~ 2000 cm^{-1} are observed. In a 5C distorted square pyramidal site, the excited state splitting (Δ^5E) increases, and transitions are observed at approximately 10 000 cm^{-1} and 5000 cm^{-1}. Transitions in a 5C trigonal bipyramidal site are shifted to lower energy, and are typically observed at < 10 000

cm^{-1} and < 5000 cm^{-1}. Due to lower values of 10 Dq, LF transitions of 4C distorted tetrahedral ferrous sites are observed at low energy, usually between 4000 and 7000 cm^{-1}. Thus, near-IR MCD spectra probe the ^5E excited state and provide information on the geometric and electronic structure of the ferrous active site.[55]

Two ligand field (d-d) transitions are observed in the MCD spectrum of resting TH-[ ], shown in Figure 5A, that can be resolved into two Gaussian bands centered at 8720 cm^{-1} and 10 750 cm^{-1}. The pattern of two bands centered around 10 000 cm^{-1} split by 2030 cm^{-1} is typical of 6C distorted octahedral ferrous sites. The MCD spectrum of TH-[L-tyr], shown in Figure 5B, appears to be slightly narrower than that of resting TH. The TH-[L-tyr] spectrum is best fit with two Gaussian bandshapes at 9390 cm^{-1} and 10 950 cm^{-1} with the higher energy band less intense. Figure 5C shows the MCD spectrum for TH-[6MPH$_4$].[56] This spectrum is also narrower than the resting TH spectrum. However, the spectrum cannot be fit with only one band, and is best fit with one band at 9250 cm^{-1} and another less intense band at approximately 10 800 cm^{-1} (the position of this band is dependent on the intensity distribution of the two Gaussians used to fit the spectrum). Thus, the MCD spectra of TH-[L-tyr] and TH-[6MPH$_4$] are consistent with both species having distorted 6C geometries with slightly stronger ligand fields (10 $Dq \sim 400$ cm^{-1} higher in energy) and less axial distortion (smaller Δ^5E) compared to TH-[ ]. These results are consistent with the XAS results (*vide supra*) which show that resting, substrate, or cofactor bound forms of TH are 6C.

In contrast, TH-[L-tyr,6MPH$_4$] shows only one band at 8960 cm^{-1} (Figure 5D),[57] suggesting that the second band of the ^5E has shifted to below the cutoff of the MCD instrument, and the Fe^{II} site has gone 5C when both substrate and cofactor are present. This is supported by the variable-temperature-variable-field (VTVH) MCD results in the next section and is consistent with the XAS results (*vide supra*). The $< 10 000$ cm^{-1} energy of the band would support a trigonal bipyramidal site; however, analysis of VTVH MCD data gives a +ZFS system (*vide infra*) which indicates that the site is closer to square pyramidal.[55,58,59] The shift of the transition to less than 10 000 cm^{-1} suggests a strong axial perturbation to the iron site which would decrease the equatorial ligand field.

VTVH MCD—While MCD spectra probe the Fe^{II} ^5E exited state, the splittings of the $^5T_2$ ground state can be obtained by VTVH MCD. The field and temperature dependence of the normalized MCD intensity of the TH complexes are plotted against $\beta H/2kT$ (where β is the Bohr magnetron, H is magnetic field in Tesla, k is Boltzmann's constant, and T is temperature in Kelvin) in Figure 5E-H. The resulting isotherms are nested (non-superimposed) and this nesting behavior can be used to gain insight into the ground state electronic structure of the Fe^{II} sites.[28,58,60] The three-fold orbitally degenerate $^5T_{2g}$ ground state will split in energy in the low symmetry protein environment. This splitting can be defined in terms of an axial splitting of the d$_{xy}$ from the d$_{xz,yz}$ orbitals by an amount Δ, and rhombic splitting of the d$_{xz}$ and d$_{yz}$ orbitals by an amount $|V|$. The resultant orbitally non-degenerate ground state is still five-fold degenerate in spin (S = 2), and undergoes a zero-field splitting (ZFS), due to spin-orbit coupling of the low symmetry split components of the $^5T_2$ state, to yield $M_S = \pm 2, \pm 1$ and 0 sublevels split by 3D and D, where D is the axial ZFS parameter. Systems with weak axial ligand fields have negative ZFS (D < 0) and the $M_S \pm 2$ doublet is the lowest energy (Figure 6, top right). This will further split by an amount δ due to the rhombic ZFS splitting of the $^5T_2$. When a magnetic field is applied, the splitting of the $M_S = \pm 2$ non-Kramers doublet increases due to the Zeeman effect (g$_\parallel\beta$H) and shows non-linear dependence on magnetic field due to a change of its wavefunction (Figure 6, bottom right). Simulations show that magnitude of δ is directly proportional to the degree of nesting of MCD isotherms.[61] For positive ZFS systems (D > 0, Figure 6, top left) which corresponds to strong a axial LF perturbation of the $^5T_2$, the $M_S = 0$ sublevel is lowest in energy. When a perpendicular magnetic field is applied, it interacts with one component of the $M_S = \pm 1$, which is D cm^{-1} above it in energy. The

resulting pseudo-doublet will Zeeman split and behave similarly to the $M_S \pm 2$ doublet in the −ZFS case to yield similar non-linear field dependence (Figure 6, bottom left). In general, + ZFS systems, which are split by the large axial ZFS (D), have much larger nesting behavior than −ZFS systems.[55,61]

The spin-Hamiltonian parameters can be obtained from VTVH MCD data by computationally fitting the field and temperature dependence of the normalized MCD intensity, taking into consideration linear B-terms, z-polarization, and thermal population of states (Equation 1 in Ref. 55). Once δ and $g_{//}$ (and D and $g_{//}$ for +ZFS) are known, they can be used [58] to obtain and |V|, the axial and rhombic splitting of the t_2 set of d orbitals. All the TH VTVH MCD data were fit with both − ZFS and + ZFS models, which can be distinguished from each other by comparing the spin-Hamiltonian values obtained. In particular, +ZFS systems will give non-physical, low $g_{//}$ values (vs $g_{//}$ = 8.8 – 10 cm^{-1} for − ZFS 6C), and a low-lying excited state singlet when fit to a − ZFS model.[58]

From Figure 5E, the saturation data of the TH-[ ] bands exhibit a very small nesting and can be fit with a − ZFS model giving spin-Hamiltonian parameters of δ = 3.1 cm^{-1} and $g_{//}$ = 9.1 cm^{-1}. These yield $^5T_2$ ground state parameters of Δ = −200 cm^{-1} and |V| = 60 cm^{-1}. The doublet ground state and small splitting of the t_{2g} d orbitals are typical of a 6C Fe^{II} site with moderate rhombic distortion (|$V/2\Delta$| ~ 0.15). The splitting of the $^5T_2$ ground state is combined with the excited state splitting (Δ^5E = 2030 cm^{-1}, from the MCD spectrum) to give the experimental d-orbital energy level diagram for TH-[ ] (Figure 7, left).

The VTVH MCD data for TH-[L-tyr] (Figure 5F) show increased nesting compared to resting TH, but are still described as a − ZFS system with δ = 5.4 cm^{-1}, $g_{//}$ = 9.0 cm^{-1} to yield Δ= −250 cm^{-1} and |V| = 130 cm^{-1}. The large δ and relatively small Δ are consistent with an Fe^{II} site with a higher degree of rhombicity (|$V/2\Delta$| = 0.26), and thus a larger splitting of the t_2 orbitals is observed. The excited state data presented earlier shows that tyrosine binding shifts the e orbitals to higher energy (10 Dq = 10,170 cm^{-1}), and decreases their splitting to 1560 cm^{-1}. Overall, the experimental orbital energy levels for TH-[L-tyr] (Figure 7, second panel) are consistent with a distorted 6C iron site.

The VTVH data of TH-[6MPH$_4$] also show more nesting than that of resting TH and fit equally well to both − ZFS and + ZFS models (Information Figure S5). A larger total splitting of the orbitals of the ground state is observed when pterin binds to the enzyme regardless of the sign of the ZFS (Figure 7, third panel). However, from the XAS data (*vide supra*) that TH-[6MPH$_4$] is 6C, which is consistent with a −ZFS. The parameters for the doublet ground state (− ZFS) in TH-[6MPH$_4$] are δ = 3.7 cm^{-1}, $g_{//}$ = 9.2 cm^{-1}, Δ= −500 and |V| = 220 cm^{-1}. The orbitals of the ^5E excited state of TH-[6MPH$_4$] are also shifted to higher energy, suggesting an overall stronger 6C LF at the Fe^{II} center relative to resting.

The saturation behavior of TH-[L-tyr, 6MPH$_4$] is dramatically different from TH-[ ]. The saturation curves are significantly more nested, and must be fit with a + ZFS system. The ground state of TH-[L-tyr, 6MPH$_4$] is now M_S = 0 and gives D = 11.2 cm^{-1}, |E| = 2.6 cm^{-1}, Δ = 700 cm^{-1} and |V| = 420 cm^{-1}. The large t_2 orbital splittings and + ZFS for TH-[L-tyr, 6MPH$_4$] are consistent with a 5C site that is closer to square pyramidal in geometry. The ground state analysis yields |$V/2\Delta$| = 0.3, indicating a high degree of rhombic distortion. In addition, the excited state transitions for TH-[L-tyr, 6MPH$_4$] occur at 8960 cm^{-1} and < 5000 cm^{-1}, a range consistent with a 5C site with a strong axial distortion. Although there is no crystal structure of this ternary complex of TH, the MCD data of PAH are very similar and examination of the structure of PAH with cofactor and substrate analog bound (PDB ID 1MMT [16]) shows a 5C Fe^{II} site that has one short axial bond and rhombically distorted equatorial ligand field

(Figure 8). Excited and ground state parameters obtained from MCD spectra and VTVH analyses of the four TH complexes are summarized in Table 3.

TH mutants: E332A and S395A—The S395A-[ ] spectrum, shown in Figure 9A (brown) has a shape very similar to wild-type TH-[ ], but is almost two-fold more intense. The spectrum is fit well with two Gaussian bands at 8850 cm^{-1} and 10,870 cm^{-1}, and the saturation behavior of the LF bands shows small nesting (Figure 9B) and fits to a −ZFS system. Together, these indicate that the iron site in S395A-[ ] is distorted 6C. As in wild-type TH, the substrate + cofactor bound form of S395A has only one resolvable transition (9330 cm^{-1}) in its MCD spectrum (Figure 9C tan). Also, as with the WT enzyme, the VTVH data of S395A-[L-tyr, 6MPH$_4$] (Figure 9D) show a large increase in nesting and yield a + ZFS system, showing that the active site has become 5C square pyramidal.

The MCD spectrum of E332A-[ ] (Figure 10A, purple) shows two bands centered around 10 000 cm^{-1}, but looks qualitatively quite different from that of wild-type TH. The intensity ratios of the 2 bands are reversed — the higher energy band now has more intensity than the lower energy band. The Gaussian-resolved band positions are 8880 cm^{-1} and 10 610 cm^{-1} and give Δ^5E of 1830 cm^{-1}. The smaller excited state splitting suggests less distortion of this 6C site than in resting wild-type TH. The saturation data (Figure 10B) of this mutant show small nesting and are fit to a − ZFS system, confirming that the ferrous site is 6C. When both substrate and cofactor are bound to E332A, the MCD spectrum changes to show only one band (9150 cm^{-1} Figure 10C, light blue). The VTVH data of this band (Figure 10D) again exhibit very large nesting and yield a + ZFS system, confirming that the iron site in E332A-[L-tyr, 6MPH$_4$] is 5C distorted square pyramidal.

The ligand field, spin-Hamiltonian and ground state parameters for TH S395A and E332A are listed in Tables S3 and S4 in the Supporting Information.

3.3 Kinetics

Stopped-flow single-turnover kinetic experiments were performed on WT and E332A TH to further probe the mechanism of the reaction of TH with pterin and O$_2$. The oxidation of Fe^{II}TH to Fe^{III}TH results in a broad increase in the absorbance spectrum between 200 and 450 nm (Figure 11A), corresponding to a ligand to Fe^{III} charge transfer transitions.[37] In addition, the reduced and oxidized pterin species have distinctive absorbance spectra over the same wavelength region (Figure 11B); these can be used to identify pterin-based intermediates formed during the reaction. In the rapid kinetic experiments, the oxidation of Fe^{II} was followed as absorbance increases at 246 and 350 nm (Figure 11A, black to orange). The oxidation of 6MPH$_4$ to quinonoid 6MPH$_2$ (q-6MPH$_2$) is uniquely characterized by increased absorbance at 350 – 450 nm (solid red to dashed green in Figure 11B). The formation of 4a-HO-6MPH$_3$ from 6MPH$_4$ was detected by absorbance changes at two diagnostic wavelengths: a maximal initial absorbance increase at 246 nm and an accompanying decrease at 300 – 340 nm (solid red to dotted blue in Figure 11B). The slow dehydration of 4a-HO-6MPH$_3$ to q-6MPH$_2$ is accompanied by a decrease at 246 nm and an increase at 300 – 450 nm (blue to green in Figure 11B).

Representative stopped-flow absorbance traces from the reactions of different TH complexes (~100 μM final concentration) with varied concentrations of O$_2$ (95 μM to 950 μM) at 5 °C are shown in Figures 12 and 13, and S7–S10. All the reactions could be successfully simulated using one of the mechanisms in Scheme 3. The rate constants used in the simulations are summarized in Table 4. Addition of O$_2$ to resting Fe^{II}TH-[ ] results in monophasic absorbance increases at 246 nm and 350 nm (Figure 12, dashed red trace) with a single step second-order mechanism with a rate constant of 0.037 $mM^{-1}s^{-1}$ (Scheme 3A, Table 4 and Figure S7), in agreement with previous studies at 20 °C.[37] Similarly, the oxidation of 6MPH$_4$ to q-6MPH$_2$

in the presence of apo-TH is well-described as a single second-order reaction with a rate constant of 1.7×10^{-4} mM^{-1}s^{-1} (Table 4), comparable to the rate of tetrahydropterin auto-oxidation in solution under the same conditions (1.3×10^{-4} mM^{-1}s^{-1}, results not shown).

The absorbance changes accompanying the reaction with oxygen of TH complexes containing substrates or analogs are more complex. All are better described by an initial reversible oxygen binding step to form Enz:O$_2$ complexes followed by chemical transformations (Schemes 3B & C and Figures S8 – S10). The presence of tyrosine or 6MPH$_2$ has little effect on the kinetics of Fe^{II} oxidation (Figure 12). The Fe^{II}TH-[5-deaza-6MPH$_4$] complex is an exception; in this case, the rate constants are the same as for Fe^{II}TH-[6MPH$_2$], but the magnitudes of the absorbance changes are much smaller and are consistent with the amount of the free enzyme in these samples (Figure 12, grey dotted and black solid lines, respectively), suggesting that binding of 5-deaza-6MPH$_4$ to TH significantly decreases the reactivity with oxygen.

The rate constant for Fe^{II} oxidation in the Fe^{II}TH-[6MPH$_4$] complex is about 5-fold faster than that for the other binary complexes containing the redox-inactive pterins. This suggests that a change in the oxidation state of the pterin accompanies oxidation of the Fe^{II}. Scheme 3B, in which the reaction of O$_2$ with Fe^{II}TH-[6MPH$_4$] results in concomitant oxidation of FeII to Fe^{III} and 6MPH$_4$ to 6MPH$_3^{\bullet}$ in the first step, followed by disproportionation of 6MPH$_3^{\bullet}$ to give q-6MPH$_2$ and 6MPH$_4^{\bullet}$, accounts well for the absorbance traces at 246 nm and 350 nm (Figures 12 and S9). The rate constant for 6MPH$_4$ oxidation in the Fe^{II}TH-[6MPH$_4$] complex shows a three order of magnitude acceleration over the auto-oxidation reaction in apo-TH-[6MPH$_4$] (0.16 s^{-1} vs 1.7×10^{-4} s^{-1}, respectively). The mechanism of Scheme 3B is consistent with the redox potentials of the individual species. Using an E^0 of $+ 210$ mV for the Fe^{II} in TH,[62] the 1-electron oxidation of Fe^{2+} + O$_2$ → Fe^{3+} + O$_2^{-\bullet}$ (O$_2$ + e$^-$ → O$_2^{-\bullet}$, E^0 = -330 mV) [63] has E^0 = -537 mV and is uphill by 12.5 kcal/mol.. Similarly, the reaction of 6MPH$_4$ to 6MPH$_3^{\bullet}$H+ (E^o = -270 mV)[64] with O$_2$ has E^0 = -600 mV and is energetically uphill by 14 kcal/mol. However, the two electron reaction between Fe^{2+}, O$_2$ and 6MPH$_4$, (O$_2$ + 2e$^-$ → H$_2$O$_2$, E^0 = $+ 280$ mV)[63] has E^0 = $+ 83$ mV, and is downhill at $- 1.9$ kcal/mol. Taken together, all these results indicate that the concerted 2-electron transfer to O$_2$ from 6MPH$_4$ and Fe^{II} (equation 1) is more favorable than the individual 1-electron oxidation processes.

$$Fe^{2+} + O_2 + 6MPH_4 \rightarrow Fe^{3+} + H_2O_2 + 6MPH_3^{\bullet} \tag{1}$$

When O$_2$ is mixed with Fe^{II}TH-[L-tyr,6MPH$_4$] to form a catalytically competent complex, a reversible oxygen complex is initially formed with no observable absorbance change. This is followed by biphasic absorbance changes at 246 nm, 318 nm and 330 nm over approximately 4 s (Figure 13, dashed green trace). This rapid initial first phase corresponds to the formation of 4a-OH-6MPH$_3$ with a rate constant of 24 s^{-1} (Scheme 3C and Figure S10). The 4a-OH-6MPH$_3$ is formed in the same step as the Fe^{IV}=O intermediate (Schemes 2 and 3C). Rapid-quench Mössbauer spectroscopy has previously shown that the Fe^{IV}=O intermediate is also formed with a rate constant of 24 s^{-1} under the same conditions used here.[26] The slower second phase was successfully modeled as the release of 4a-OH-6MPH$_3$ from the enzyme active site into the solution with a rate constant of 0.42 s^{-1} (Figure S10), a value which matches k$_{cat}$ under these conditions. The 4a-OH-6MPH$_3$ subsequently dehydrates in solution to produce q-6MPH$_2$, resulting in a gradual decrease at 246 nm and increases at 318 nm and 330 nm, with a rate constant of ~0.02 s^{-1}. The reactions of O$_2$ with Fe^{II}TH-[L-tyr,5-deaza-6MPH$_4$] and FeIITH-[L-tyr,6MPH$_2$], which presumably have similar 5C sites,[65] are similar to Fe^{II} oxidation in Fe^{II}TH with either 6MPH$_2$ or tyrosine bound (Figure 13A and Table 4). This indicates that both a 5C Fe^{II} and a redox active pterin are needed for the two (and greater)

orders of magnitude rate enhancement in the reactivity with O_2 seen with $Fe^{II}TH$-[L-tyr, $6MPH_4$] compared to FeIITH-[ ], $Fe^{II}TH$-[L-tyr], and $Fe^{II}TH$-[$6MPH_4$].

The absorbance changes upon addition of O_2 to E332A-$Fe^{II}TH$-[L-tyr,$6MPH_4$] are shown in Figure 13 (solid blue traces). The enzyme clearly catalyzes a reaction between Fe^{II}, O_2 and pterin, but the absorbance changes are distinct from those seen with WT $Fe^{II}TH$-[L-tyr, $6MPH_4$]. In the case of the E332A mutant, the observed absorbance changes can be accounted for by initial reversible oxygen addition followed by formation of an intermediate in a single slow step with a rate constant of $0.3 \ s^{-1}$; this value matches k_{cat} for this mutant enzyme. The intermediate decays nonenzymatically with almost the same rate constant ($\sim0.02 \ s^{-1}$) as the dehydration of 4a-HO-$6MPH_3$ to q-$6MPH_2$. The reaction catalyzed by the E332A mutant is clearly slower than that of the wild-type enzyme. The rate constant for the second step is similar to the rate constant for release of the 4a-HO-$6MPH_3$ from the wild-type enzyme. This raises the possibility that the observed rate constant is a net rate constant which includes formation of the intermediate and its release from the enzyme; however, these two rate constants are too similar to resolve. Compared to WT TH, the magnitudes of the absorbance changes at 246 nm and 330 nm and the sign of the absorbance change at 318 nm after O_2 binding are different for E332A TH (Figure 13, solid blue traces). The spectrum of the intermediate could be obtained by global analysis of the absorbance changes between 240 and 450 nm, fitting the data to a three step kinetic model (Figure S11). The starting spectrum and those of the final two species match those for $6MPH_4$, q-$6MPH_2$, and 7,8-$6MPH_2$. The spectrum of the unknown intermediate exhibits a number of differences from that of 4a-HO-$6MPH_3$, including a much lower absorbance at 246 nm and a red-shifted absorbance maximum. These differences establish that, in contrast to WT TH, a 4a-HO-pterin is not formed in the reaction of E332A-$Fe^{II}TH$ [L-tyr, $6MPH_4$] with O_2. However, the decay of the intermediate in the E332A TH reaction to q-$6MPH_2$ with a rate constant nearly identical to that for 4a-HO-$6MPH_3$ suggests that this intermediate is similar to it. Spectral differences similar to those between this intermediate and that of 4a-HO-$6MPH_3$ have been observed previously for 4a-HO- and 4a-HOO-flavins, intermediates in the reaction of the flavoprotein phenol hydroxylases.[66,67] Thus, a possible candidate for this intermediate species in the E332A TH reaction is a hydroperoxy-pterin, HOO-$6MPH_3$.[67]

The rapid single-turnover kinetics experiments presented above allow the dissection of individual steps of TH reaction, and show that the presence of a 5C Fe^{II} site and a redox-active pterin greatly accelerates the enzyme reaction with O_2. The data on the WT vs E332A reactions also provide insights into the nature of the intermediates formed in the coupled vs uncoupled reaction.

4 Discussion

In this study, we present new spectroscopic insight and information on the catalytically relevant ferrous active site of TH and its interaction with tyrosine and 6-methyltetrahydropterin ($6MPH_4$). XAS and MCD studies show that the FeII active site is 6C in resting TH. The geometric and electronic structure of the Fe^{II} site is slightly perturbed when either tyrosine or pterin is bound to TH, but the site remains 6C in both cases. The active site goes 5C when both tyrosine and pterin are bound, opening up a coordination position for the O_2 reaction. The EXAFS data for TH-[L-tyr,$6MPH_4$] are also consistent with a 5C FeII site with 2 His, 1 bidentate Glu and 1 water as ligands, comparable to the crystal structure determined for Fe^{II}-PAH with thienylalanine and BH_4 bound (PDB 1KWO[17]). The 6C $\rightarrow$ 5C change in the TH active site is consistent with the general mechanistic strategy observed in other non-heme iron enzymes that use redox-active cofactors to activate O_2 for reaction with substrates.[28,60,68]

Earlier steady-state kinetic studies on WT TH were consistent with an ordered binding sequence of pterin followed by oxygen in rapid equilibrium and then tyrosine before the DOPA product is released.[18] This result suggested that the Fe^{II} site in TH could undergo different structural changes upon pterin binding which allow the Fe^{II}, pterin and O_2 to react before tyrosine binds. The protein itself does undergo conformational changes upon pterin binding.[69] However, our spectroscopic data show only a slight perturbation to the 6C Fe^{II} site upon pterin binding. While steady-state experiments give information on the overall reaction, they do not provide information on individual mechanistic steps.[70] In addition, these experiments were complicated by the use of a large excess of $6MPH_4$, required to ensure steady-state conditions, because the excess $6MPH_4$ also reduces the Fe. Here, we have used single-turnover kinetics experiments with tyrosine and $6MPH_4$ (added in stoichiometric amounts to minimize side reactions) to evaluate the individual steps and identify short-lived intermediates in the TH reaction.

The single turnover kinetic results indicate that the isolated one-electron oxidation reactions of Fe^{II} to Fe^{III} in $Fe^{II}TH$-[ ] and tetrahydropterin to quinonoid dihydropterin (q-$6MPH_2$) in apoTH-[$6MPH_4$] are slow due to unfavorable thermodynamics. However, the combination of Fe^{II} and redox-active pterin in $Fe^{II}TH$-[$6MPH_4$] accelerates both the FeII and uncoupled pterin oxidation reactions, even though the Fe^{II} site remains 6C. The faster reaction rates in $Fe^{II}TH$-[$6MPH_4$] can be ascribed to the favorable thermodynamics of the two-electron reduction of O_2 to peroxide by the combined reaction of $Fe^{II} \rightarrow Fe^{III}$ and $6MPH_4 \rightarrow 6MPH_3^\bullet$. When both pterin and tyrosine are bound to give a 5C $Fe^{II}TH$ site, the first observable step in the O_2 reaction, corresponding to the breakdown of the putative Fe^{II}-OO-pterin intermediate, is $2 - 3$ orders of magnitude faster than the Fe^{II}, $6MPH_4$ and $Fe^{II} + 6MPH_4$ oxidation reactions in the 6C and non-catalytic 5C forms of TH (Table 4). The measured rate constant for this step necessarily sets a lower limit for the rate constant for the initial reaction with oxygen to form this intermediate. Thus the two electron transfer from the 5C Fe^{II} and reduced pterin to O_2 is far more favorable than in the 6C $Fe^{II}TH$-[$6MPH_4$] site and than in the 5C FeIITH-[L-tyr,5-deaza-$6MPH_4$] and $Fe^{II}TH$-[L-tyr,$6MPH_2$] sites, confirming that *the open coordination position on the FeII and the presence of a redox active pterin are both critical for catalytic TH reactivity*.

In an earlier study on PAH mutants related to phenylketonuria (PKU), structural differences in the active site were observed that suggested that the pterin will react with O_2 to make peroxypterin which decays in the uncoupled reaction to give off H_2O_2.[32] Here, we are able to observe individual reaction steps in the coupled WT and uncoupled E332A reactions when both tyrosine and $6MPH_4$ are bound. The first step with observable kinetics in WT TH is the decay of this putative intermediate, which occurs at a rate of 24 s^{-1}. The 4a-OH-pterin that forms in WT TH (and in the S395A mutant) is not observed in the E332A mutant, which also does not hydroxylate tyrosine, indicating that the $Fe^{IV}=O$ intermediate also does not form. The first observable step of the E332A TH reaction is the formation of an oxidized pterin species, possibly the HOO-pterin, with a rate constant of 0.3 s^{-1}. This intermediate may form either by direct reaction of O_2 with $6MPH_4$ (however this reaction is much slower at 1.7×10^{-4} $mM^{-1}s^{-1}$), or, more likely, through a Fe^{II}-OO-pterin intermediate as in WT TH. In the latter case, the E332A mutation may change the reactivity of the Fe^{II}-OO-pterin intermediate such that it decomposes with a slower rate and through a different mechanism than WT. In both, decay of the intermediate likely involves protonation of the Fe^{II}-OO-pterin. In WT TH, the nature of the cleavage products, $Fe^{IV}=O$ and 4a-OH-pterin indicate that the O distal (O_{dis}) to the FeII is protonated to heterolytically cleave (Scheme 4, top). In the E332A mutant, an oxidized pterin species, possibly the HOO-pterin, is formed. This would involve the protonation of the O proximal to Fe (O_{prox}) in the FeII-OO-pterin, followed by the cleavage of the Fe-O_{prox} bond (Scheme 4, bottom). These results suggest that the E332 residue

participates in the reactivity of TH by directing the distal protonation of the Fe^{II}-OO-pterin intermediate.

The crystal structure of Fe^{II}-PAH with thienylalanine and tetrahydrobiopterin bound (PDB 1KW0, Figure 14)[17] indicates that the E332 carboxylate group is oriented towards the pterin, and could hydrogen bond to it, either through direct interaction with the proton on the N3, or through solvent molecules. The E332 residue could either directly transfer the proton from N3 to O_{dis} (N3 is deprotonated in the final quinonoid pterin product), or direct a solvent water via an H-bond to the O_{dis}. The water ligand is not likely to be the proton source for heterolytic O-O cleavage, because the MCD data of the TH-[L-tyr, $6MPH_4$] complexes in WT and E332A indicate that the geometric and electronic structures of the 5C sites are very similar (Figure 10C). Apparently, when E332 is mutated to an alanine, the enzyme can no longer direct a proton to O_{dis}, and the O_{prox} is protonated instead, leading to the cleavage of the Fe-O bond to regenerate Fe^{II} and HOO-pterin.

In summary, we have shown through XAS and MCD spectroscopy that the Fe^{II} active site in TH is 6C until both tyrosine and pterin are bound. This $6C \rightarrow 5C$ conversion is consistent with the general mechanistic strategy observed in other mononuclear non-heme iron enzymes. Single turnover kinetic data on WT TH indicate that at a 6C active site, the two electron reduction of O_2 to peroxide by Fe^{II} and pterin is favored over individual one electron reactions. However, this reaction is still slow. Importantly, this reaction is greatly accelerated in the Fe^{II}TH-[L-tyr, $6MPH_4$] complex, indicating that both 5C FeII and pterin are required for the O_2 reaction. Comparison of the kinetics of WT and E332A TH-[L-tyr, $6MPH_4$] reactions with O_2 indicate that the E332 residue plays a role in directing the protonation of the bridged Fe^{II}-OO-pterin complex to produce the Fe^{IV}=O hydroxylating intermediate and hence is important for tuning the TH active site for productive coupled turnover. Application of the spectroscopic and mechanistic analyses described in this study to variants of TH related to neurological disorders would provide molecular-level insight into enzyme dysfunction and define potential therapeutic approaches.

Supplementary Material

Refer to Web version on PubMed Central for supplementary material.

Acknowledgments

7 References and Notes

1. Fitzpatrick PF. Annu Rev Biochem 1999;68:355–381. [PubMed: 10872454]

2. Hufton SE, Jennings IG, Cotton RGH. Biochem J 1995;311:353–366. [PubMed: 7487868]

3. Kappock TJ, Caradonna JP. Chem Rev 1996;96:2659–2756. [PubMed: 11848840]

4. Lüdecke B, Knappskog PM, Clayton PT, Surtees RAH, Clelland JD, Heales SJR, Brand MP, Bartholomé K, Flatmark T. Hum Mol Genet 1996;5:1023–1028. [PubMed: 8817341]

5. Smyth C. Amer J Pysch 1996;153:271–274.

6. Ludecke B, Dworniczak B, Bartholomé K. Hum Genet 1995;95:123–125. [PubMed: 7814018]

7. Royo M, Daubner SC, Fitzpatrick PF. Proteins 2005;58:14–21. [PubMed: 15468323]

8. Kaufman S. Adv Enzymol Relat Areas Mol Biol 1993;67:77–264. [PubMed: 8322620]

9. Shiman, R. Chemistry and Biochemistry of Pterins. Blakley, RL.; Benkovic, SJ., editors. Vol. 2. John Wiley & Sons; New York: 1985. p. 179-249.

10. Kuhn DM, Ruskin B, Lovenberg W. J Biol Chem 1980;255:4137–4143. [PubMed: 7372670]

11. Volner A, Zoidakis J, Abu-Omar MM. J Biol Inorg Chem 2003;8:121–128. [PubMed: 12459906]

12. Pember SO, Johnson KA, Villafranca JJ, Benkovic SJ. Biochemistry 1989;38:2124–2130. [PubMed: 2719947]

13. Loeb KE, Westre TE, Kappock TJ, Mitic N, Glasfeld E, Caradonna JP, Hedman B, Hodgson KO, Solomon EI. J Am Chem Soc 1997;119:1901–1915.

14. Kemsley JN, Mitic N, Loeb Zaleski K, Caradonna JP, Solomon EI. J Am Chem Soc 1999;121:1528–1536.

15. Wasinger EC, Mitic N, Hedman B, Caradonna J, Solomon EI, Hodgson KO. Biochemistry 2002;41:6211–6217. [PubMed: 12009881]

16. Andersen OA, Stokka AJ, Flatmark T, Hough E. J Mol Biol 2003;333:747–757. [PubMed: 14568534]

17. Anderson OA, Flatmark T, Hough E. J Mol Biol 2002;320:1095–1108. [PubMed: 12126628]

18. Fitzpatrick PF. Biochemistry 1991;30:3658–3662. [PubMed: 1673058]

19. Goodwill KE, Sabatier C, Marks C, Raag R, Fitzpatrick PF, Stevens RC. Nat Struct Biol 1997;4:578–585. [PubMed: 9228951]

20. Goodwill KE, Sabatier C, Stevens RC. Biochemistry 1998;37:13437–13445. [PubMed: 9753429]

21. Meyer-Klaucke W, Winkler H, Schünemann V, Trautwein AX, Nolting HF, Haavik J. Eur J Biochem 1996;241:432–439. [PubMed: 8917440]

22. Ramsey AJ, Hillas PJ, Fitzpatrick PF. J Biol Chem 1996;271:24395–24400. [PubMed: 8798695]

23. Dix TA, Benkovic SJ. Acc Chem Res 1988;21:101–107.

24. Dix TA, Bollag GE, Domanico PL, Benkovic SJ. Biochemistry 1985;24:2955–2958. [PubMed: 4016080]

25. Dix TA, Kuhn DM, Benkovic SJ. Biochemistry 1987;26:3354–3361. [PubMed: 2888478]

26. Eser BE, Barr EW, Frantom PA, Saleh L, Bollinger JM Jr, Krebs C, Fitzpatrick PF. J Am Chem Soc 2007;129:11334–11335. [PubMed: 17715926]

27. Fitzpatrick PF. Biochemistry 2003;42:14083–14091. [PubMed: 14640675]

28. Solomon EI, Brunold TC, Davis MI, Kemsley JN, Lee SK, Lehnert N, Neese F, Skulan AJ, Yang YS, Zhou J. Chem Rev 2000;100:235–349. [PubMed: 11749238]

29. Kovaleva EG, Lipscomb JD. Nat Chem Biol 2008;4:186–193. [PubMed: 18277980]

30. Bassan A, Blomberg MRA, Siegbahn PEM. Eur J Biochem 2003;9:106–114.

31. Valliancourt FH, Labbe G, Drouin NM, Fortin PD, Eltis LD. J Biol Chem 2002;277:2019–2027. [PubMed: 11707443]

32. Kemsley JN, Wasinger EC, Datta S, Mitic N, Acharya T, Hedman B, Caradonna JP, Hodgson KO, Solomon EI. J Am Chem Soc 2003;125:5677–5686. [PubMed: 12733906]

33. Dickson PW, Jennings IG, Cotton RGH. J Biol Chem 1994;269:20369–20375. [PubMed: 7914195]

34. Erlandsen H, Bjorgo E, Flatmark T, Stevens RC. Biochemistry 2000;39:2208–2217. [PubMed: 10694386]

35. Ellis HR, Daubner SC, Fitzpatrick PF. Biochemistry 2000;39:4174–4181. [PubMed: 10747809]

36. Daubner SC, Fitzpatrick PF. Biochemistry 1999;38:4448–4454. [PubMed: 10194366]

37. Frantom PA, Seravalli J, Ragsdale SW, Fitzpatrick PF. Biochemistry 2006;45:2372–2379. [PubMed: 16475826]

38. Ramsey AJ, Daubner SC, Ehrlich JI, Fitzpatrick PF. Protein Sci 1995;4:2082–2086. [PubMed: 8535244]

39. Moad G, Luthy CL, Benkovic PA, Benkovic SJ. J Am Chem Soc 1979;101:6068–6076.

40. Source: SSRL Biological XAS beam line 7–3, 20-pole, 2-Tesla wiggler, 0.8 mrad beam; SPEAR3 at 3 GeV, 85–100 mA. Optics: Si(220), liquid nitrogen cooled double crystal monochromator, fully tuned, with a flat, bent, harmonic-rejection vertically collimating Rh coated Si pre-monochromator M_0 mirror at 9 keV cutoff; energy resolution 1×10^{-4} $\Delta E/E$.

41. Source: SSRL Biological XAS beam line 9–3, 16-pole, 2-Tesla wiggler, 2.0 mrad beam, SPEAR3 at 3 GeV, 85–100 mA. Optics: Si(220), liquid nitrogen cooled double crystal monochromator, fully tuned. Pre-monochromator flat, bent, harmonic rejection vertically collimating Rh coated Si M0 mirror; and post-monochromator bent, cylindrical, Rh coated Si focusing M_1 mirror; 10 keV cutoff, energy resolution 1×10^{-4} $\Delta E/E$.

42. Scott RA, Hahn JE, Doniach S, Freeman HC, Hodgson KO. J Am Chem Soc 1982;104:5364–5369.

43. Cramer SP, Tench O, Yochum M, George GN. Nucl Instrum Methods Phys Rev 1988;A266:586–591.

44. Cramer SP, Hodgson KO. Prog Inorg Chem 1979;25:1–39.

45. DeWitt JG, Bentsen JG, Rosenzweig AC, Hedman B, Green J, Pilkington S, Papaefthymiou GC, Dalton H, Hodgson KO, Lippard SJ. J Am Chem Soc 1991;113:9219–9235.

46. Scott RA. Methods Enzymol 1985;177:414–459.

47. Tenderholt A, Hedman B, Hodgson KO. AIP Conference Proceedings 2007;882:105–107.

48. George, GN. Stanford Linear Acceleration Center. Stanford University; Stanford, CA: EDG_FIT; Stanford Synchrotron Radiation Laboratory; p. 94309

49. Goodwill KE, Sabatier C, Marks C, Raag R, Fitzpatrick PF, Stevens RC. Nat Struc Biol 1997;4:578–585.

50. George, GN. Stanford Linear Acceleration Center. Stanford University; Stanford, CA: EXAFSPAK; Stanford Synchrotron Radiation Laboratory; p. 94309

51. Kuzmic P. Anal Biochem 1996;237:260–273. [PubMed: 8660575]

52. Westre TE, Kennepohl P, DeWitt JG, Hedman B, Hodgson KO, Solomon EI. J Am Chem Soc 1997;119:6297–6314.

53. Randall CR, Shu L, Chiou YM, Hagen KS, Ito M, Kitajima N, Lachicotte RJ, Zang Y, Que L Jr. Inorg Chem 1995;34:1036–1039.

54. Pavlosky MA, Zhang Y, Westre TE, Gan QF, Pavel EG, Campochiaro C, Hedman B, Hodgson KO, Solomon EI. J Am Chem Soc 1995;117:4316–4327.

55. Pavel EG, Kitajima N, Solomon EI. J Am Chem Soc 1998;120:3949–3962.

56. The MCD spectrum of TH-[5deaza-6MPH$_4$] is shown in Supporting Information (Figure S4). This normalized spectrum overlays with that of TH-[6MPH4], indicating that the spectral changes are independent of the nature of the pterin cofactor. This also allows the comparison of the TH[cofactor] spectra to the PAH-^{R}[cofactor] spectrum (ref 13), which shows much less perturbation compared to PAH-^{T}[ ]. .

57. We also attempted to fit the MCD spectrum of Fe^{II}TH[tyr,6MPH$_4$] with two bands (Figure S6 in Supporting Information), but the best resultant does not improve the fit to data. In addition, the two Gaussian bands used in the best fit have widths of ~ 1500 cm^{-1}, narrower than the ~ 2000 cm^{-1} required to fit all other ferrous d-d bands. Moreover, the two Gaussian bands used in the fit have an energy separation of ~ 1000 cm^{-1}, which is too small to be associated with a single ferrous center, where the minimum splitting is the ~ 1400 cm^{-1} that would occur in a very symmetric 6C environment (Jones, G. D.; *Phys. Rev*. 1967, 155, 256–261). .

58. Solomon EI, Pavel EG, Loeb KE, Campochiaro C. Coord Chem Rev 1995;144:369–460.

59. A recent Mossbauer study on Fe^{II} TH-[tyr,6MPH$_4$] shows an asymmetric signal, indicating that two distinct Fe^{II} complexes ($\sim 80:20$ ratio) are present (ref 26). However, the second minor Fe^{II} species is not detectable in MCD, which suggests that the ligand field and geometry of the proposed minor second Fe^{II} TH-[tyr,6MPH$_4$] complex is very similar to the major Fe^{II} complex observed in the MCD samples.

60. Solomon EI. Inorg Chem 2001;40:3656–3669. [PubMed: 11442362]

61. Campochiaro C, Pavel EG, Solomon EI. Inorg Chem 1995;34:4669–4675.

62. Hagedoorn PL, Schmidt PP, Anderson KK, Hagen WR, Flatmark T, Martinez A. J Biol Chem 2001;276:22850–22856. [PubMed: 11301319]

63. Sawyer, DT. Oxygen Chemistry. Oxford University Press; New York: 1991.

64. Gorren ACF, Kungl AJ, Schmidt K, Werner ER, Mayer B. Nitric Oxide 2001;5:176–186. [PubMed: 11292367]

65. While there is no structural data on $Fe^{II}TH$-[L-tyr,5-deaza-6MPH$_4$], parallel MCD and XAS data on $Fe^{II}PAH$-[L-phe,5-deaza-6MPH$_4$] indicate that the FeII site is 5C (refs 14 and 15). Similarly, the crystal structure of $Fe^{II}PAH$-[thieylalanine, 6MPH$_2$], the PAH analog of $Fe^{II}TH$-[L-tyr,6MPH$_2$], show that the FeII site is 5C (refs 16 and 17).

66. The absorbance spectrum of 4a-OH-flavin and HOO-flavin are compared in ref 67. The λ_{max} of H-OO-flavin is shifted to lower energy and has lower ε compared to 4a-OH-flavin. A similar type of perturbation can be expected for the HOO-pterin vs 4a-OH-pterin spectra. In fact, a 2 nm red-shift is observed in the peroxy vs hydroxy adduct of 5-deaza-6MPH$_4$ by Moad et. al. (ref 39).

67. Ballou DP, Entsch B, Cole LJ. Biochem Biophys Res Comm 2005;338:590–598. [PubMed: 16236251]

68. Neidig ML, Solomon EI. Chem Commun 2005;2005:5843–5463.

69. Sura GR, Lasagna M, Gawandi V, Reinhart GD, Fitzpatrick PF. Biochemistry 2006;45:9632–9638. [PubMed: 16878998]

70. Fersht, A. W.H. Freeman; New York: 1999. p. 563
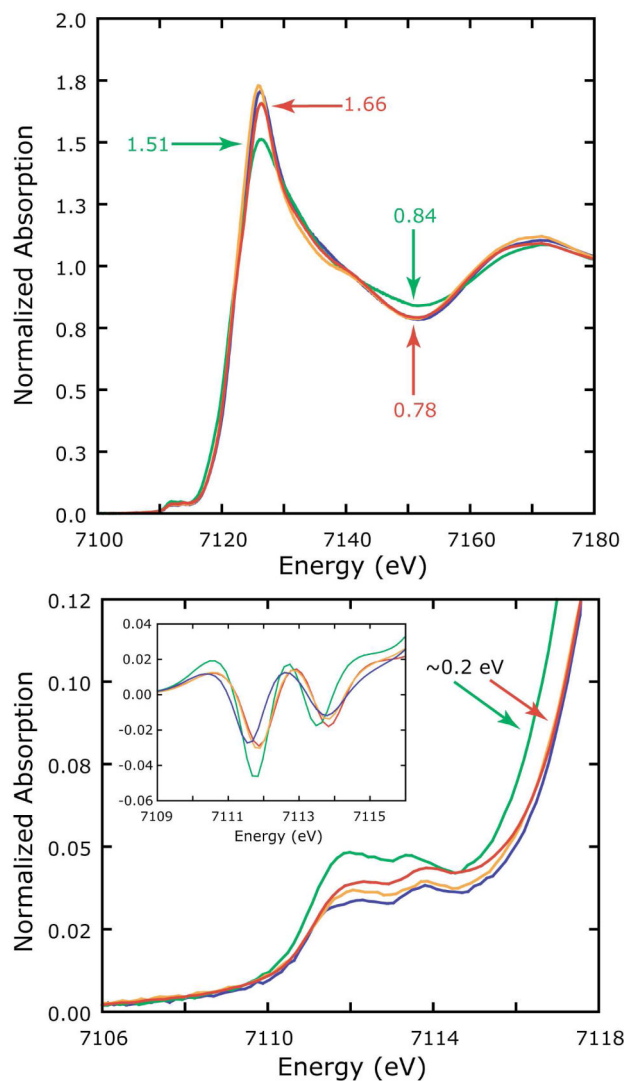
Figure 1.
Fe K edge and pre-edge spectra of TH-[ ] (red), TH-[L-tyr] (blue), TH-[6MPH$_4$] (orange) and TH-[L-tyr, 6MPH$_4$] (green). The pre-edge region has been enlarged and inset to shower finer detail over this energy region. The inset shows the smoothed 2nd derivatives of the pre-edge spectra (2nd derivative smoothed for clarity, smoothing = 0.5). A black & white version of this figure can be found in the Supporting Information, Fig S1.
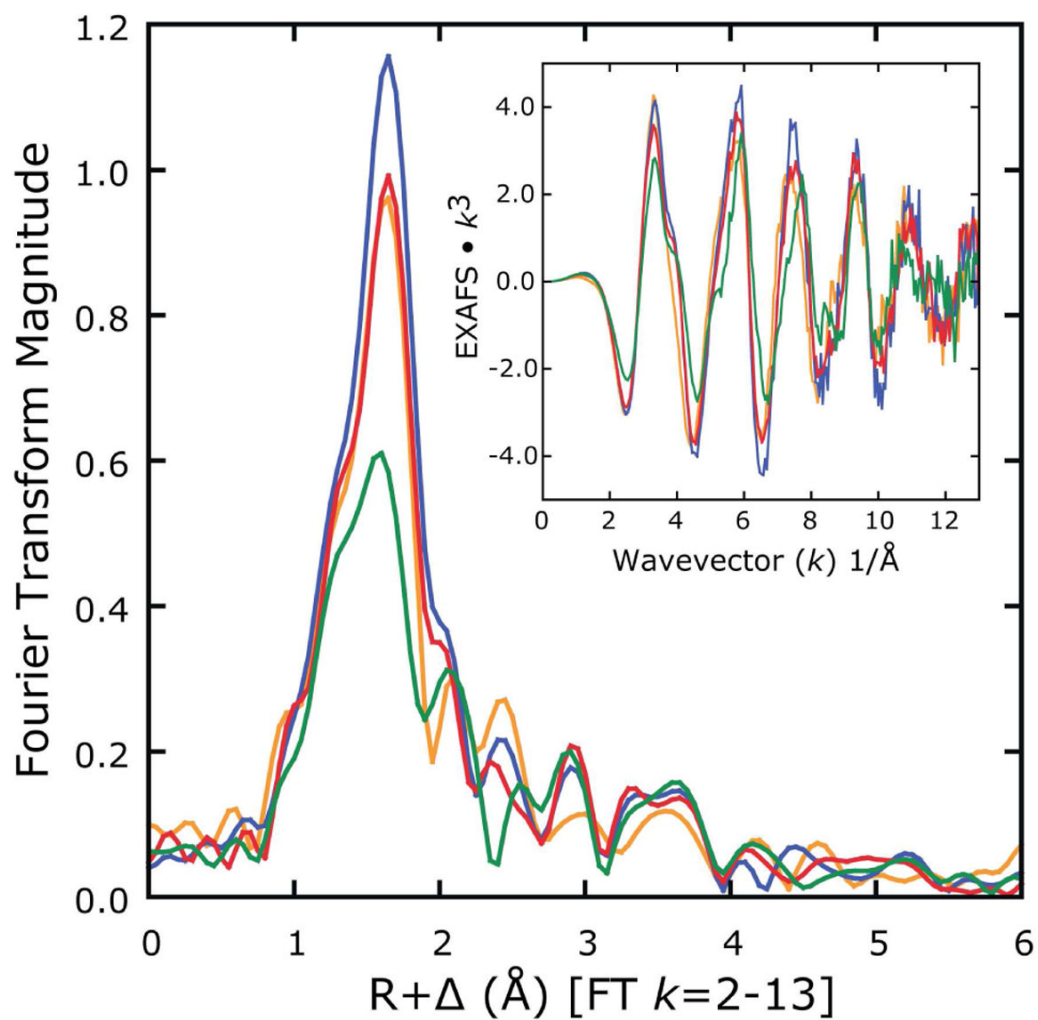
Figure 2.
Fourier transforms to $k = 13$ Å^{-1} for tyrosine hydroxylase. TH-[ ] (Red), TH-[L-tyr] (blue), TH-[6MPH$_4$] (orange) and TH-[L-tyr, 6MPH$_4$] (green). The inset shows EXAFS data for the respective samples. A black & white version of this figure can be found in the Supporting Information, Fig S2.
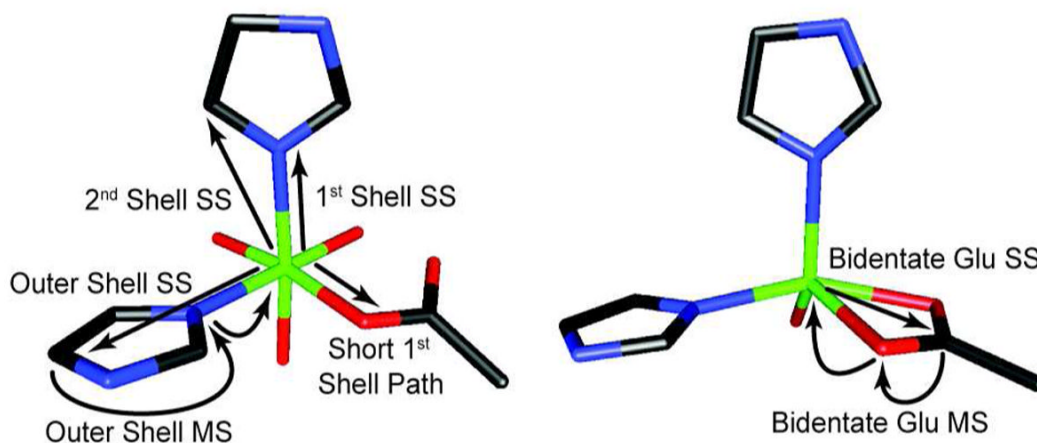
Figure 3.
Tyrosine hydroxylase active site EXAFS models. The 6C model (left), based the crystal structure of Fe^{III}TH (PDB 1TOH)[49], was used in fitting all EXAFS spectra with single (straight) and multiple (curved arrow) scattering paths shown. The 5C model (right), created from crystal structure of the ternary complex of PAH (PDB 1MMT)[16] was required for successful fitting of TH-[L-tyr, 6MPH$_4$]. This includes additional single and multiple scattering paths associated with the presence of a bidentate bound Glu. The iron is shown in green, oxygen in red, carbon in black, and nitrogen in blue.
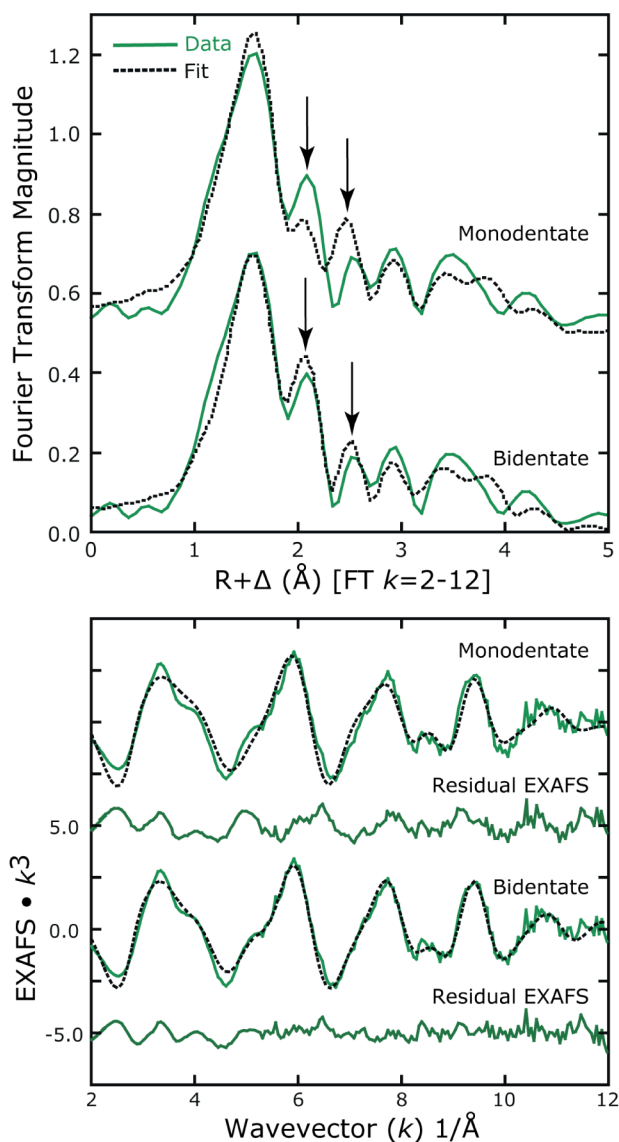
Figure 4.
Top: Fourier transform plots comparing best fits (12 and 15) for TH-[L-tyr, 6MPH$_4$] using a monodentate vs. bidentate Glu model. The monodentate Glu lacks the ~2.5 Å feature (black arrows) as shown by the residual component from the monodentate EXAFS fit (below). A bidentate model and fit including a ~2.5 Å signal with associated MS path is required to complete the fit. Bottom: *k*-space data, fit and residual corresponding to the above Fourier transforms of fits 12 (error F=0.19) and 15 (F=0.09) (Table 2). In all plots, data (—), fits (·····).
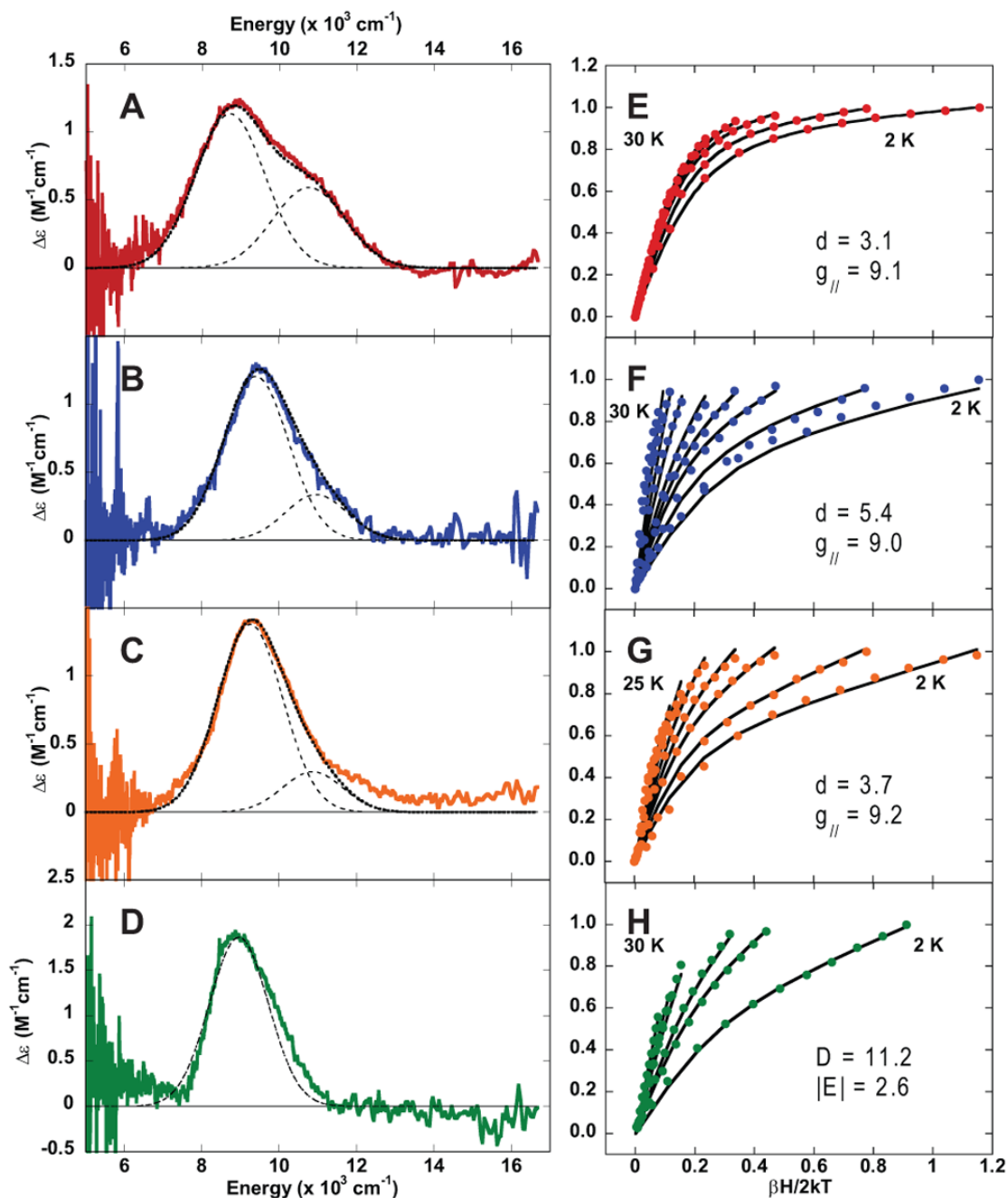
Figure 5.
Near-IR MCD spectra and saturation behavior for TH-[ ] (A & E, in red), TH-[L-tyr] (B & F, in blue), TH-[6MPH$_4$] (C & G, in orange) and TH-[L-tyr, 6MPH$_4$] (D & H in green). In A, B and C, the sum of the Gaussian-resolved bandshapes (dotted lines) yield the generated spectrum (solid black lines), which reproduce the observed spectrum well. VTVH data (points) and their best fits (—) collected at 7950 cm^{-1} for TH-[ ] (E), 8855 cm^{-1} for TH-[L-tyr] (F), 8230 cm^{-1} for TH-[6MPH$_4$] (G) and 8245 cm^{-1} for TH-[L-tyr, 6MPH$_4$] (H).
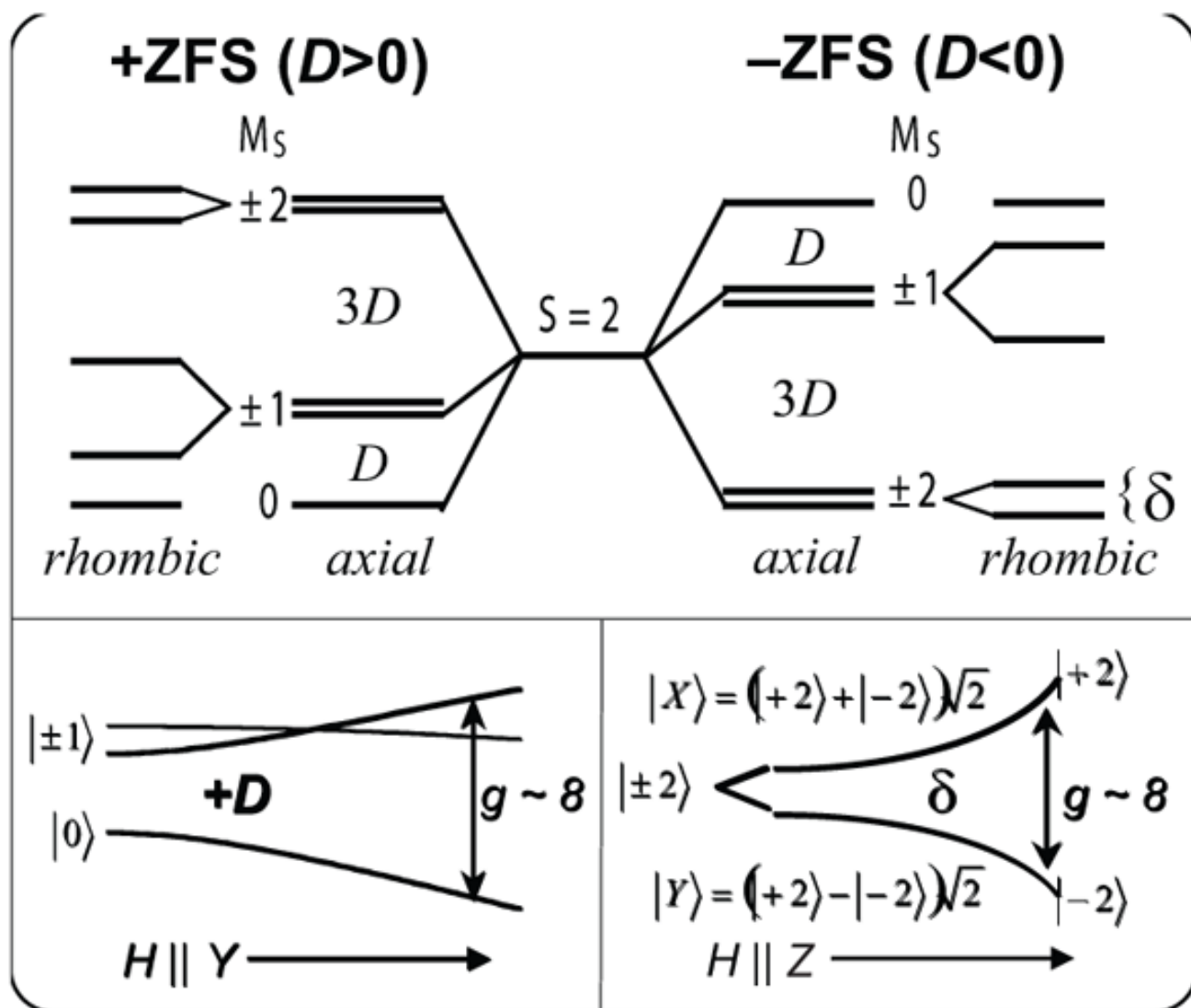
Figure 6.
Energy splittings of the S = 2 ground state for positive ZFS (top left) and negative ZFS (top right). Rhombic and magnetic field splitting and mixing of the $M_S = 0$ and one $M_S \pm 1$ component (bottom left), $M_S = \pm 2$ non-Kramers doublet (bottom right).

WT TH d-orbitals
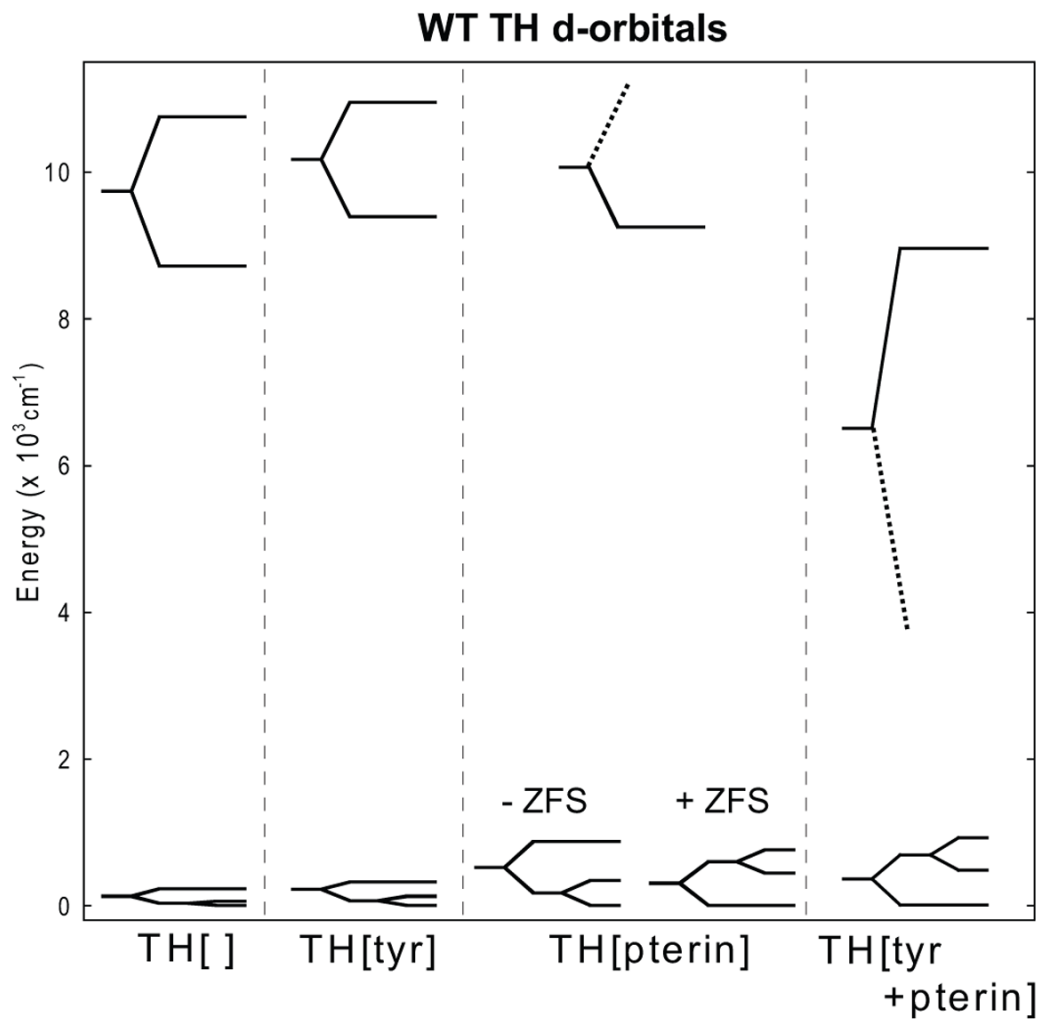
Figure 7.
Experimental d-orbital energies of Fe^{II}TH complexes. The excited state splittings are obtained from band positions in the NIR-MCD spectra, and ground state splittings from VTVH MCD. Dotted lines represent uncertainty in energy positions of the orbitals.
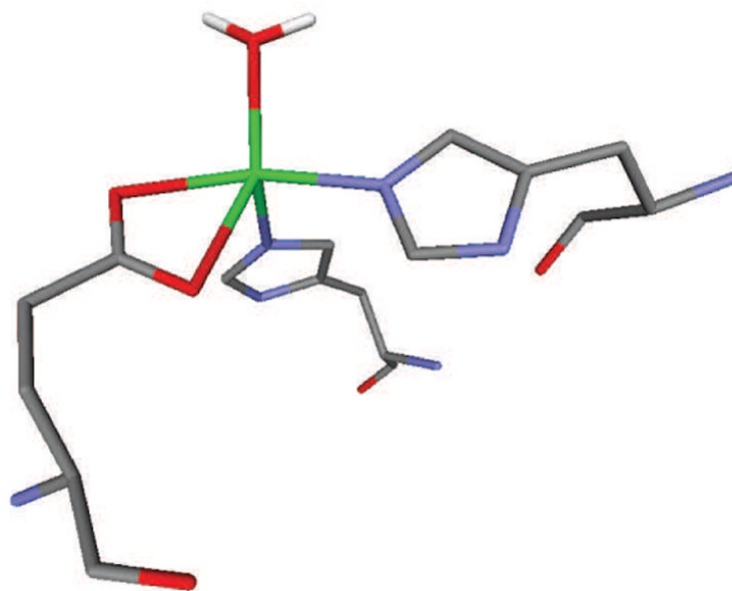
Figure 8.
Geometry of Fe^{II} site in PAH with substrate analog and cofactor bound (PDB 1MMT)[16], showing a rhombically distorted equatorial ligand field and a short Fe-OH$_2$ bond.
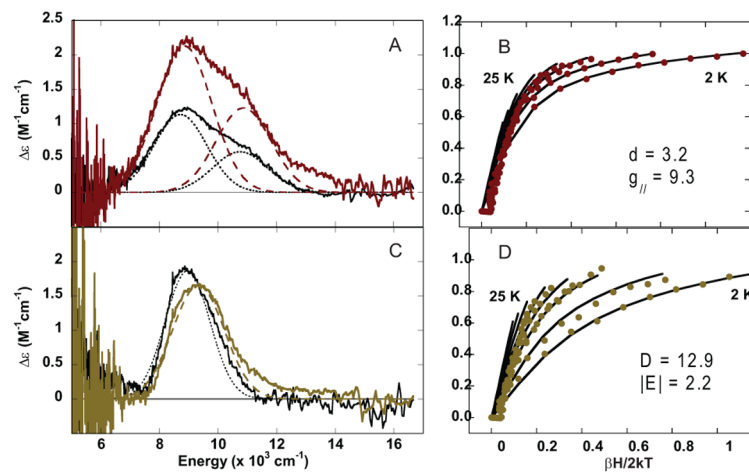
Figure 9.
MCD spectra at 5K and 7T of S395A mutant. Gaussian-resolved bandshapes for each spectrum are shown in dashed lines. (A) S395A-[ ] (brown) compared to WT TH-[ ] (black), (B) VTVH data (●) and fit (—) of S395A-[ ] collected at 7830 cm^{-1}, (C) S395A-[L-tyr, 6MPH$_4$] (tan) compared to WT TH-[L-tyr, 6MH$_4$] (black), (D) VTVH data (●) and fit (—) of S395A-[L-tyr, 6MPH$_4$] collected at 8333 cm^{-1}.
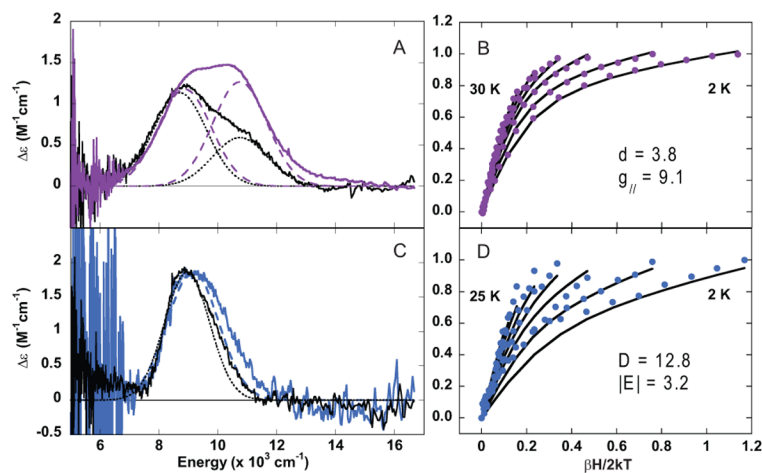
Figure 10.
MCD spectra at 5K and 7T of E332A mutant. Gaussian-resolved bandshapes for each spectrum are shown in dashed lines. (A) E332A-[ ] (purple) compared to WT TH-[ ] (black), (B) VTVH data (●) and fit (—) of E332A-[ ] collected at 8650 cm^{-1}, (C) E332A-[L-tyr, 6MPH$_4$] (light blue) compared to WT TH-[L-tyr, 6MH$_4$] (black), (D) VTVH data (●) and fit (—) of E332A-[L-tyr, 6MPH$_4$] collected at 8306 cm^{-1}.
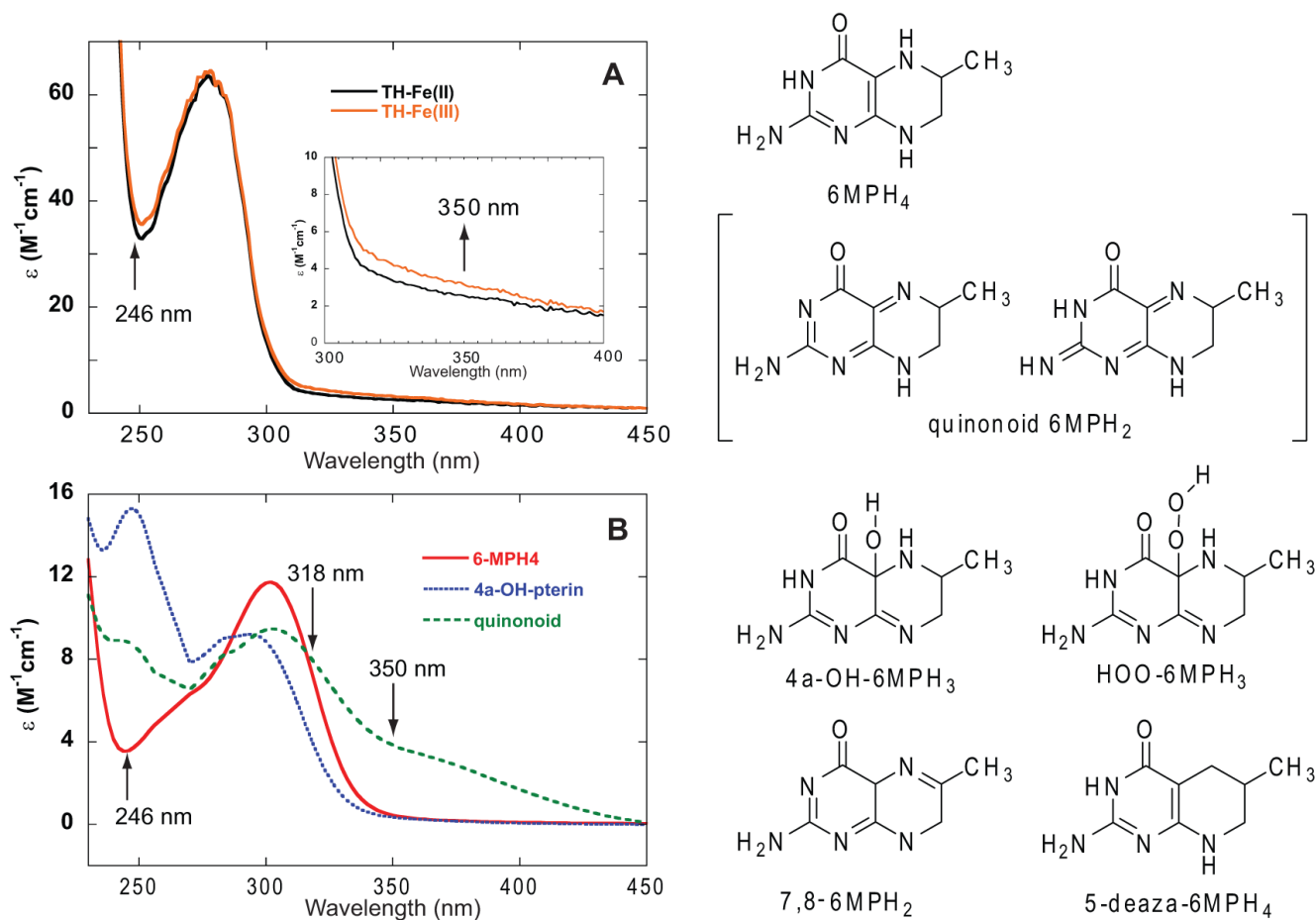
Figure 11.
Left, absorbance spectra of $Fe^{II}TH$ (A) and pterin species (B) at neutral pH. Right, structures of pterin species.
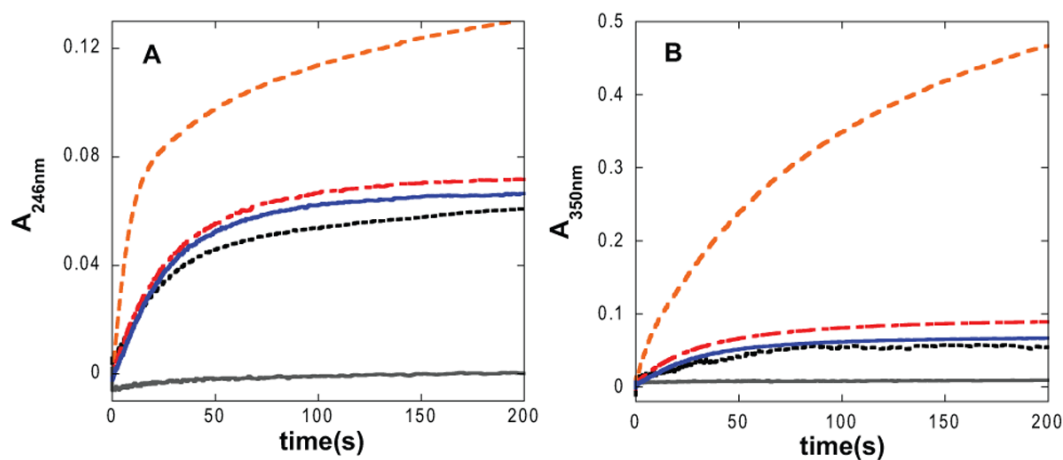
Figure 12.
Kinetic traces at 246 nm (A) and 350 nm (B) upon mixing a final concentration of 950 μM O_2 with the following $Fe^{II}TH$ complexes (90 to 140 μM): $Fe^{II}TH$-[ ] (dashed red line), $Fe^{II}TH$-[6MPH$_4$] (dashed orange line), $Fe^{II}TH$-[5-deaza-6MPH$_4$] (solid grey line), $Fe^{II}TH$-[L-tyr] (solid blue line) and $Fe^{II}TH$-[6MPH$_2$] (dotted black line).
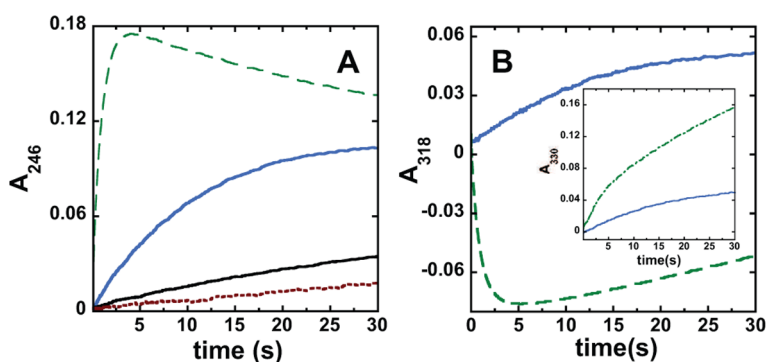
Figure 13.
Kinetic traces at 246 nm (A) and at 318 nm and 330nm (inset) (B) upon mixing a final concentration of 95 uM O_2 with the following Fe^{II}TH complexes: 150 μM WT TH-[L-tyr, 6MPH$_4$] (dashed green line), 150 μM E332A TH-[L-tyr,6MPH$_4$] (light blue line), 100 μM WT TH-[L-tyr,5-deaza-6MPH$_4$] (dotted brown line) and 120 μM WT TH-[L-tyr,6MPH$_2$] (solid black line).
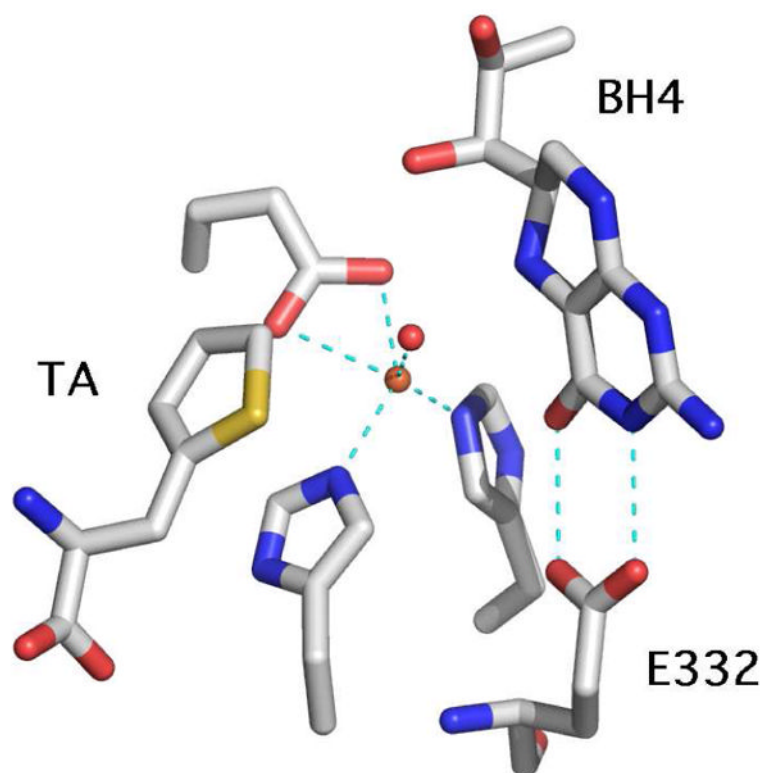
Figure 14.
Crystal structure of the Fe^{II} active site of PAH showing the binding positions of the amino acid substrate (TA, thienylalanine, cofactor (BH4, tetrahydrobiopterin), metal ligands and the E332 residue (using the TH numbering). The figure was created from the PDB file 1KW0.[17]
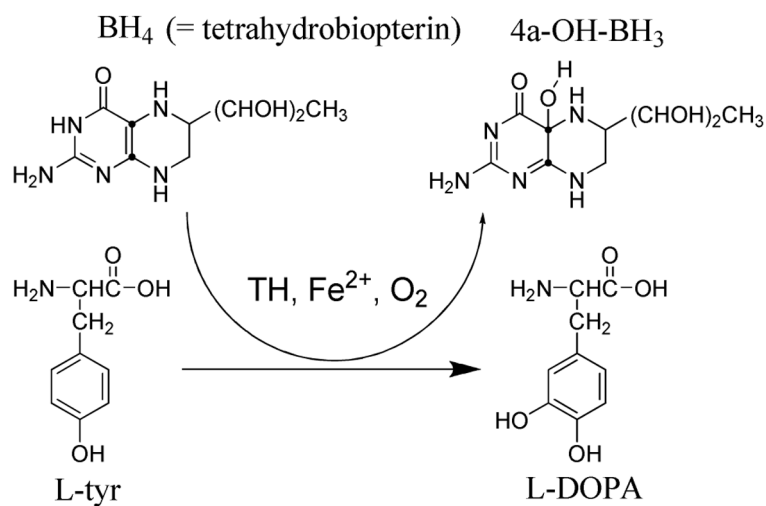
Scheme 1.
The pterin-dependent reaction catalyzed by TH.
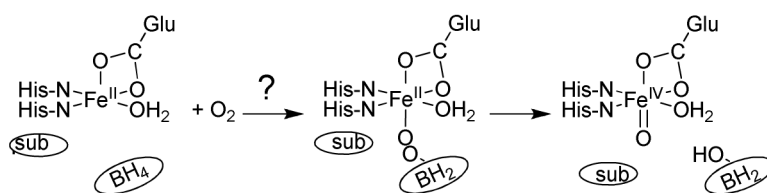
Scheme 2.
Proposed mechanism for the formation of $Fe^{IV}=O$ intermediate. (BH_4 = tetrahydrobiopterin)

A. $\text{TH-Fe(II)}\ +\ \text{O}_2\ \xrightarrow{\ 0.037\ \text{mM}^{-1}\text{s}^{-1}\ }\ \text{TH-Fe(III)}$

B. $\text{TH-Fe(II)-6MPH}_4\ +\ \text{O}_2\ \underset{0.5\text{s}^{-1}}{\overset{1.5\ \text{mM}^{-1}\text{s}^{-1}}{\rightleftarrows}}\ \text{TH-Fe(II)-6MPH}_4\text{-O}_2$

$\text{TH-Fe(II)-6MPH}_4\text{-O}_2\ \xrightarrow{\ 0.16\ \text{s}^{-1}\ }\ \text{TH-Fe(III)}\ +\ \text{6MPH}_3^\bullet\ +\ \text{H}_2\text{O}_2$

$\text{6MPH}_3^\bullet\ +\ \text{6MPH}_3^\bullet\ \xrightarrow{\ 40\ \text{mM}^{-1}\text{s}^{-1}\ }\ \text{6MPH}_4\ +\ \text{q-6MPH}_2$

C. $\text{TH-Fe(II)-6MPH}_4\text{-tyr}\ +\ \text{O}_2\ \underset{50\ \text{s}^{-1}}{\overset{300\ \text{mM}^{-1}\text{s}^{-1}}{\rightleftarrows}}\ \text{TH-Fe(II)-6MPH}_4\text{-tyr-O}_2$

$\text{TH-Fe(II)-6MPH}_4\text{-tyr-O}_2\ \xrightarrow{\ 24\ \text{s}^{-1}\ }\ \text{TH-Fe(IV)=O-tyr}\ +\ \text{4a-HO-6MPH}_3$

$\downarrow\qquad\qquad\qquad\qquad\downarrow\ \text{- H}_2\text{O}$

$\text{TH:Fe(II)}\ +\ \text{DOPA}\qquad\text{q-6MPH}_2$

D. $\text{E332A TH-Fe(II)-6MPH}_4\text{-tyr}\ +\ \text{O}_2\ \underset{3\ \text{s}^{-1}}{\overset{10\ \text{mM}^{-1}\text{s}^{-1}}{\rightleftarrows}}\ \text{E332A TH-Fe(II)-6MPH}_4\text{-tyr-O}_2$

$\text{E332A TH-Fe(II)-6MPH}_4\text{-tyr-O}_2\ \xrightarrow{\ 0.3\ \text{s}^{-1}\ }\ \text{E332A TH-Fe(II)-tyr}\ +\ \text{4a-HOO-6MPH}_3$

$\downarrow\ \text{- H}_2\text{O}_2$

q-6MPH_2

Scheme 3.
Reactions of various TH complexes with O_2

$$Fe^{II}\text{-}O\text{-}O\text{-}PH_2 \xrightarrow[H^+]{\begin{array}{c}WT\\[1ex]E332A\end{array}} \begin{array}{c} Fe^{II}\text{-}O\text{-}\overset{H}{O}\text{-}PH_2 \longrightarrow Fe^{IV}{=}O + HO\text{-}PH_3 \\[3ex] Fe^{II}\text{-}\overset{H}{O}\text{-}O\text{-}PH_2 \longrightarrow Fe^{II} + HOOH\text{-}PH_3 \end{array}$$

Scheme 4.
Proposed protonation sites in WT and E332A TH
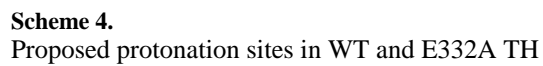
Table 1

XAS pre-edge energies and intensities

Sample	Peak (eV)	Area	Total Intensity
TH-[ ]	7112.0	4.4	8.3 ± 0.6
	7113.8	3.9	
TH-[L-tyr, 6MPH$_4$]	7111.8	6.4	12.5 ± 1.5
	7113.5	6.1	
TH-[6MPH$_4$]	7111.9	4.6	8.2 ± 0.7
	7113.8	3.6	
TH-[L-tyr]	7111.9	4.4	8.5 ± 1.0
	7113.7	4.1	

Pre-edge fit values obtained using EDG_FIT according to established methods.[48] Peak energies are listed at peak maximum, areas are multiplied by 100 for comparison to other data. Total intensity is the sum of both areas. Error values calculated from total intensity standard deviations across all 9 fits per sample.

Table 2

EXAFS fits.

TH-[ ] – Resting

	fit 1 (E$_0$= −4.0)			fit 2 (E$_0$= −3.8)			fit 3 (E$_0$ = −3.8)		
	CN	R(Å)	σ²(Å²)	CN	R(Å)	σ²(Å²)	CN	R(Å)	σ²(Å²)
Fe-O/N	---	---	---	---	---	---	1	2.10	375
Fe-O/N	6	2.15	678	5	2.15	556	5	2.17	725
C SS	4	3.12	774	4	3.12	776	4	3.12	725
C SS	4	4.08	817	4	4.08	737	4	4.08	797
C-N MS	8	4.39	951	8	4.40	979	8	4.40	961
Error			0.15			0.16			0.15

TH-[$_L$-tyr] – Substrate

	fit 4 (E$_0$= −3.5)			fit 5 (E$_0$= −3.4)			fit 6 (E$_0$= −3.8)		
	CN	R(Å)	σ²(Å²)	CN	R(Å)	σ²(Å²)	CN	R(Å)	σ²(Å²)
Fe-O/N	---	---	---	---	---	---	1	2.14	542
Fe-O/N	6	2.16	567	5	2.16	457	5	2.16	598
C SS	4	3.11	657	4	3.11	645	4	3.10	666
C SS	4	4.07	785	4	4.07	730	4	4.07	827
C-N MS	8	4.40	1168	8	4.41	1177	8	4.39	1132
Error			0.22			0.31			0.21

TH-[6MPH$_4$] – Cofactor

	fit 7 (E$_0$= −4.5)			fit 8 (E$_0$= 4.3)			fit 9 (E$_0$ = −3.7)		
	CN	R(Å)	σ²(Å²)	CN	R(Å)	σ²(Å²)	CN	R(Å)	σ²(Å²)
Fe-O/N	---	---	---	---	---	---	1	2.11	172

TH-[ ] – Resting

	fit 1 ($E_0 = -4.0$)			fit 2 ($E_0 = -3.8$)			fit 3 ($E_0 = -3.8$)		
	CN	R(Å)	σ^2(Å^2)	CN	R(Å)	σ^2(Å^2)	CN	R(Å)	σ^2(Å^2)
Fe-O/N	6	2.17	758	5	2.17	630	5	2.20	785
C SS	4	3.07	809	4	3.08	791	4	3.08	816
C SS	4	4.09	787	4	4.08	719	4	4.08	654
C-N MS	8	4.35	1045	8	4.36	1132	8	4.36	1210
Error		0.29			0.34			0.25	

TH-[L-Tyr, 6MPH$_4$] – Active Monodentate Glu Model

	fit 10 ($E_0 = -4.1$)			fit 11 ($E_0 = -3.8$)			fit 12 ($E_0 = -4.3$)		
	CN	R(Å)	σ^2(Å^2)	CN	R(Å)	σ^2(Å^2)	CN	R(Å)	σ^2(Å^2)
Fe-O/N	---	---	---	---	---	---	1	2.00	411
Fe-O/N	6	2.13	1127	5	2.13	932	4	2.15	567
C SS	4	3.11	663	4	3.11	602	4	3.10	664
C SS	4	4.07	886	4	4.06	818	4	4.06	867
C-N MS	8	4.37	778	8	4.38	771	8	4.37	769
Error		0.27			0.20			0.19	

TH-[L-Tyr, 6MPH$_4$] – Active Bidentate Glu Model

	fit 13 ($E_0 = -4.9$)			fit 14 ($E_0 = -4.6$)			fit 15 ($E_0 = -4.3$)		
	CN	R(Å)	σ^2(Å^2)	CN	R(Å)	σ^2(Å^2)	CN	R(Å)	σ^2(Å^2)
Fe-O/N	---	---	---	1	2.04	408	2	2.05	578
Fe-O/N	5	2.14	943	4	2.17	782	3	2.15	628
C SS	1	2.54	336	1	2.50	342	1	2.53	372
C-O MS	4	2.63	336	4	2.68	342	4	2.65	372
C SS	4	3.10	708	4	3.10	821	4	3.11	733
C SS	4	4.05	794	4	4.05	745	4	4.05	760

TH-[ ] – Resting

	fit 1 ($E_0 = -4.0$)			fit 2 ($E_0 = -3.8$)			fit 3 ($E_0 = -3.8$)		
	CN	R(Å)	σ^2(Å^2)	CN	R(Å)	σ^2(Å^2)	CN	R(Å)	σ^2(Å^2)
C-N MS	8	4.38	810	8	4.38	823	8	4.39	769
Error			0.12			0.12			0.09

Select fit parameters for TH XAS EXAFS samples. All distances are in Å. σ^2 values are multiplied by 10^5 for convenience. SS and MS indicate single and multiple scattering pathways, respectively.

Error (F) is defined as $F = \Sigma[(\chi exp - \chi obsd)^2 k^6]/\Sigma(\chi exp 2k^6)$.

Table 3

Excited state transition energies, spin-Hamiltonian and ground state parameters for $Fe^{II}TH$ complexes. Values are in cm^{-1}.

Sample	Band 1	Band 2	10 Dq	Δ^5E	d	g//	D	|E|	Δ	|V|	V/2Δ
TH-[ ]	8720	10 750	9735	2030	3.1	9.1	-	-	−200	60	0.15
TH-[L-tyr]	9390	10 950	10 170	1560	5.4	9	-	-	−250	130	0.26
TH[6MPH$_4$]	9250	~10 900	~10 100	1610	3.7	9.2	-	-	−500	220	0.22
					5.6	8.0	11.4	2.4	600	324	0.27
TH[L-tyr, 6MPH$_4$]	8960	-	-	> 4000	5.2	8.0	11.2	2.6	700	420	0.30

Table 4

Rate constants for the reactions of WT and E332A TH complexes with O_2 at 5 °C.

	$Fe^{II}TH + O_2 \rightarrow Fe^{III}TH (mM^{-1}s^{-1})$			
$Fe^{II}TH-[\ ]$	0.037			

	$Fe^{II}TH + O_2 \leftrightarrow Fe^{II}TH:O_2$		$Fe^{II}TH:O_2 \rightarrow$ $Fe^{III}TH$ (s^{-1})	$6MPH_4 \rightarrow$ $q\text{-}6MPH_2$ $(mM^{-1}s^{-1})$
	k_{on} (mM^{-1}s^{-1})	k_{off} (s^{-1})		
$Fe^{II}TH-[6MPH_4]$	1.5	0.5	0.16	40
apoTH-$[6MPH_4]$				0.00017
$Fe^{II}TH-[5\text{-}deaza\text{-}6MPH_4]$			No reaction	
$Fe^{II}TH-[6MPH_2]$	2.0	0.5	0.032	
$Fe^{II}TH-[L\text{-}tyr]$	2.0	0.5	0.040	
$Fe^{II}TH-[5\text{-}deaza\text{-}6MPH_4, L\text{-}tyr]$	2.0	0.4	0.026	
$Fe^{II}TH-[6MPH_2, L\text{-}tyr]$	6.0	0.5	0.050	

			$Fe^{II}TH:O_2 \rightarrow Fe^{IV}=O + 4a\text{-}HO\text{-}6MPH_3$	
$Fe^{II}TH-[L\text{-}tyr, 6MPH_4]$	300	50	24 s^{-1}	

			$Fe^{II}TH:O_2 \rightarrow Fe^{II} + HOO\text{-}6MPH_3$	
E332A-$[L\text{-}tyr, 6MPH4]$	10	3	0.3 s^{-1}	